8-2002

Stabilization of Rutile-related Thin Film on TiO_2 Substrates

Youngnam Cho

STABILIZATION OF RUTILE-RELATED THIN FILM ON TiO_2 SUBSTRATES

By

Youngnam Cho

B.S. Dongguk University, 1997

A THESIS

Submitted in Partial Fulfillment of the

Requirements for the Degree of

Master of Science

(in Chemical Engineering)

The Graduate School

The University of Maine

August, 2002

Advisory Committee:

William J. DeSisto, Assistant Professor of Chemical Engineering, Advisor

M. Clayton Wheeler, Assistant Professor of Chemical Engineering

John C. Hassler, Professor of Chemical Engineering

STABILIZATION OF RUTILE-RELATED THIN FILM ON TiO_2 SUBSTRATES

By Youngnam Cho

Thesis Advisor: Dr. William DeSisto

An Abstract of the Thesis Presented
in Partial Fulfillment of the Requirements for the
Degree of Master of Science
(in Chemical Engineering)
August, 2002

Conducting metal oxide thin films are of broad interest because they have a wide variety of magnetic and electronic properties. Materials exist that range from superconducting to insulating, are ferromagnetic and are ferroelectric. These properties make thin conducting oxide films attractive for many industrial applications. A class of metal oxides exists that adapt the rutile crystal structure; the structure of the mineral rutile, TiO_2. These metal oxides have the general formula MO_2 where M is a metal cation of valence +4. Metal oxides crystallizing in the rutile structure also display a wide variety of physical properties. The objective of this research was to examine the ability of single crystal rutile (TiO_2) substrates to stabilize various isostructural MO_2 compounds prepared by chemical vapor deposition (CVD). This included metastable and unusual valence state metal oxide compounds. The materials examined in this thesis included CrO_2 and RuO_2.

CrO_2 is a ferromagnetic material of significant interest because it has been theoretically predicted to have complete spin-polarization of the conduction electrons. This exciting intrinsic property makes CrO_2 a leading candidate for breakthrough devices in the field of magnetoelectronics.

RuO_2 is a highly conductive oxide with metallic properties. It has attracted significant interest in the development of ultralarge scale integrated circuits as a conducting layer combined with new classes of high dielectric oxide materials. In addition, RuO_2 is an ideal non-magnetic metal layer (NM) for magnetoelectronic devices based upon CrO_2.

In order for advances in magnetoelectronics to occur using rutile-based materials, ultra thin multilayer structures must be fabricated with precise thickness and interfacial homogeneity control. A first step in realizing this goal is gaining a fundamental understanding of the thermodynamic processing space for stabilizing each compound. A second step is understanding factors which influence film roughness and physical properties. This thesis attempts to understand some of these major issues for ultimately fabricating novel magnetoelectronic devices based upon metal oxides that crystallize in the rutile structure. The characterization of the films included the crystalline structure by x-ray diffraction and surface morphology by atomic force microscopy.

ACKNOWLEDGEMENTS

I would like to thank my advisor, Dr. Bill DeSisto, for his advice through this research and for being so nice. His earnest guidance leads me to accomplish my research well. I am also grateful to all my committee members, Doctor M. Clayton Wheeler and Doctor John C. Hassler, for their support of my research. I also thank to Doctor Martin Yates, Doctor Carl Tripp, Doctor Sofian Kanan and Doctor William Unertl for showing me how to use the apparatuses. I also appreciate the assistance of LASST thin film group member and Naval Research Laboratory member for spin-polarization detection.

I would like to thank also all the graduate student as well as the professors and staffs of the chemical engineering department for being so helpful and friendly.

Finally, I would like to express my appreciation to my family, especially my husband, for their understanding and assistance and encouragement.

TABLE OF CONTENTS

ACKNOWLEDGEMENTS.....ii

LIST OF TABLES.....vi

LIST OF FIGURES.....vii

Chapter

1. INTRODUCTION.....1

1.1 Overview.....1

1.2 Organization.....3

2.MAGNETOELECTRONICS.....4

2.1 Giant magneto-resistance.....4

2.1.1 Overview.....4

2.1.2 GMR mechanisms.....5

2.1.3 Experimental observation of GMR.....8

2.2 Ferromagnetic materials.....9

2.2.1 Domain structure.....12

2.2.2 Hysteresis loop.....13

3. EXPERIMENTAL BACKGROUND.....15

3.1 Chemical vapor deposition.....15

3.1.1 Growth kinetics.....17

3.1.2 CVD reactors.....19

3.2 Thin film structural development.....21

3.3 Metal dioxide thin film with rutile-related structures.....24

3.3.1 Titanium dioxide (TiO_2).....26

3.3.2 Chromium dioxide (CrO_2).....27

3.3.3 Ruthenium dioxide (RuO_2).....28

4. PHASE-SELECTIVE CHEMICAL VAPOR DEPOSITION OF CHROMIUM OXIDES FROM CHROMYL CLORIDE.....29

4.1 Introduction.....29

4.2 Experimental technique for CrO_2 thin film deposition.....29

4.3 X-ray diffraction.....32

4.4 Results.....37

4.4.1 The crystal structure with XRD.....39

4.4.2 Thin film roughness with AFM.....45

4.4.2.1 Atomic force microscope (AFM).....46

4.4.2.2 Analysis CrO_2 thin film with growth temperature.....47

4.4.2.3 Analysis CrO_2 film with carrier gas flow rate.....49

4.4.3 $CrO_2/TiO_2/BaF_2/Si$ multilayer fabrication with chemical vapor deposition.....52

4.4.3.1 Experimental procedures.....52

4.4.3.2. Results.....52

4.4.3.2.1 The crystal structure with XRD.....52

4.4.3.2.2 The spin polarization.....54

4.5 Conclusion.....55

5. RuO_2 THIN FILM FABRICATION WITH METALORGANIC CHEMICAL VAPOR DEPOSITION....56

5.1 Introduction....56

5.2 Experimental technique for RuO_2 thin film fabrication....57

5.3 Results....59

5.4 Conclusion....65

6. CONCLUSION....66

6.1 Summary....66

6.2 Future work....68

BIBLIOGRAPHY....69

BIOGRAPHY OF THE AUTHOR....73

LIST OF TABLES

Table 3.1: The crystal data for selected MO_2 compounds with rutile-related structure ...26

Table 5.1: Deposition condition of RuO_2 thin films.....58

LIST OF FIGURES

Figure 1.1: Areal density perspective of IBM HDD products 2

Figure 2.1: Schematic representations of electron transport in layered magnetic metal structure.....7

Figure 2.2: Room temperature resistance vs magnetic field for Co/Cu and Fe/Cr multilayers.....8

Figure 2.3: A schematic representation of density of electronic states in Cu and Co.....9

Figure 2.4: Technological impact of nano scale devices fabricated with highly spin-polarized materials like CrO_2. The change in resistance measured with an applied magnetic field is plotted as a function of spin-polarization of the ferromagnetic (FM) material.....11

Figure 2.5: The magnetic moments change across the block wall between domains.....13

Figure 2.6: Hysteresis curve for ferromagnetic material.....14

Figure 3.1: Illustration showing the fundamental steps involved in the CVD.....16

Figure 3.2: Model of growth process.....17

Figure 3.3: Typical overall reaction rate for CVD reactors vs. reciprocal temperature.....19

Figure 3.4: Hot-wall CVD reactor.....20

Figure 3.5: Cold-wall CVD reactor.....20

Figure 3.6: Basic modes of thin-film growth.....21

Figure 3.7: Film classification terminology, (I) random polycrystalline, (II) polycrystalline, (III) polycrystalline with epitaxial growth, and (IV) single crystalline.....23

Figure 3.8: The rutile structure.....25

Figure 4.1: The apparatus for CrO_2 film growth.....31

Figure 4.2: The temperature distribution of reactor tube wall.....32

Figure 4.3: X-ray diffraction facility.....33

Figure 4.4: X-ray diffraction.....35

Figure 4.5: The mechanical motions of the sample and detection equipment and the motion of **q** relative to the sample for the two types of x-ray scans : a) θ/2θ scan and b) Φ scan.....36

Figure 4.6: X-ray diffraction θ/2θ scans of CrO_2 films on (a) (100) TiO_2, (b) (110) TiO_2 and (c) 001 TiO_2 substrates. The labeled peaks are CrO_2 film peaks. The substrate peaks having the corresponding indices are off-scale.....40

Figure 4.7: The phi scan on the (a) CrO_2 (100) line showing expected two-fold symmetry, (b) CrO_2(110) line showing expected two-fold symmetry, and (c) CrO_2(001) line showing expected four-fold symmetry.....42

Figure 4.8: X-ray diffraction *θ/2θ* scans of Cr_2O_3 films on (a) (0001) Al_2O_3 and (b) (1012) Al_2O_3 substrates. The labeled peaks are the Cr_2O_3 film peaks. The substrate peaks having the corresponding indices are off-scale.....43

Figure 4.9: The θ/2θ scan for (001) peak of the CrO_2 films of different thickness deposited on the (001) TiO_2 substrates.....45

Figure 4.10: AFM mechanism.....46

Figure 4.11: The rms roughness for CrO_2 thin film deposited on the TiO_2 substrate at various growth temperature. Error bars represent ±one standard deviation.....47

Figure 4.12: The surface morphology of CrO_2 film deposited on the TiO_2 substrate at two different growth temperature.....48

Figure 4.13: The rms roughness with increasing carrier gas flow rate. Error bars represent ±one standard deviation.....49

Figure 4.14: The comparison of film roughness as a function of carrier gas flow rate.....51

Figure 4.15: The XRD pattern of $CrO_2/TiO_2/BaF_2/Si$ thin film.....53

Figure 4.16: The phi scan for $CrO_2/TiO_2/BaF_2/Si$ thin film.....54

Figure 5.1: The apparatus for RuO_2 thin film on the CrO_2/TiO_2 film.....57

Figure 5.2: The procedure for measuring RuO_2 thin film on the CrO_2/TiO_2.....59

Figure 5.3: The XRD pattern of $RuO_2(001)$ film on the $CrO_2(001)/TiO_2(001)$ substrate at temperature 280°C.....60

Figure 5.4: The XRD patterns for $RuO_2(001)$ film on the $TiO_2(001)$ substrate at deposition temperature of 270 °C and 420 °C.....61

Figure 5.5: The XRD patterns of $RuO_2(001)$ film on $TiO_2(001)$ substrates at various oxygen flow rates 25 ~ 400sccm.....62

Figure 5.6: The phi scan on the RuO_2 (001) line showing expected four-fold symmetry around the (111) direction.....62

Figure 5.7: The surface morphology of RuO_2 film at various oxygen rate (a) 0sccm, (b) 25sccm, (c) 200sccm and (d) 400sccm at decomposition temperature of 320°C.....64

CHAPTER 1

INTRODUCTION

1.1 Overview

Along with continuing concern about digital information, data storage mechanisms have been developed rapidly. Innovations in the technology of data storage have driven up storage areal density to achieve a 60 percent compound annual growth rate (Fig 1).[1-3] If this growth rate continues, an areal density of 40Gbit/in^2 can be expected by 2004. High areal density can be achieved by introducing new technology, in which the most important are magnetoresistance(MR) "read head" (a magnetic field sensor for reading magnetic data) and giant magnetoresistance (GMR) technologies. The first hard drive with MR read head was introduced in 1991, which provided the highest areal density available at the time. Because the MR effect depends on the volume of sensor, an MR head's sensitivity decreases as its dimensions shrink. Fortunately, giant magneto-resistance sensors can replace MR heads with significantly advanced performance. The primary advantage in a GMR head is greater sensitivity to the magnetic field for a given head size. GMR heads are currently replacing MR heads for today's head drive technology.

GMR sensors have been used for various applications.[4-5] For example, it would be possible to replace random access memory(RAM) with magnetic RAM. Today's technology uses semiconductor RAM because it is fast, inexpensive and dense. In semiconductor based technology, RAM retains data by electrical charges on capacitor

elements. Such storage is volatile because the data must be refreshed several times a second by the electrical circuit. Using GMR, it is possible to make more attractive non-volatile magnetic RAM. Other applications of GMR include land mine sensors, power isolators, sensors in automotive applications such as ABS and air bag, and industrial sensor areas. Magnetic devices may someday complement or even replace semiconductor electronic devices.

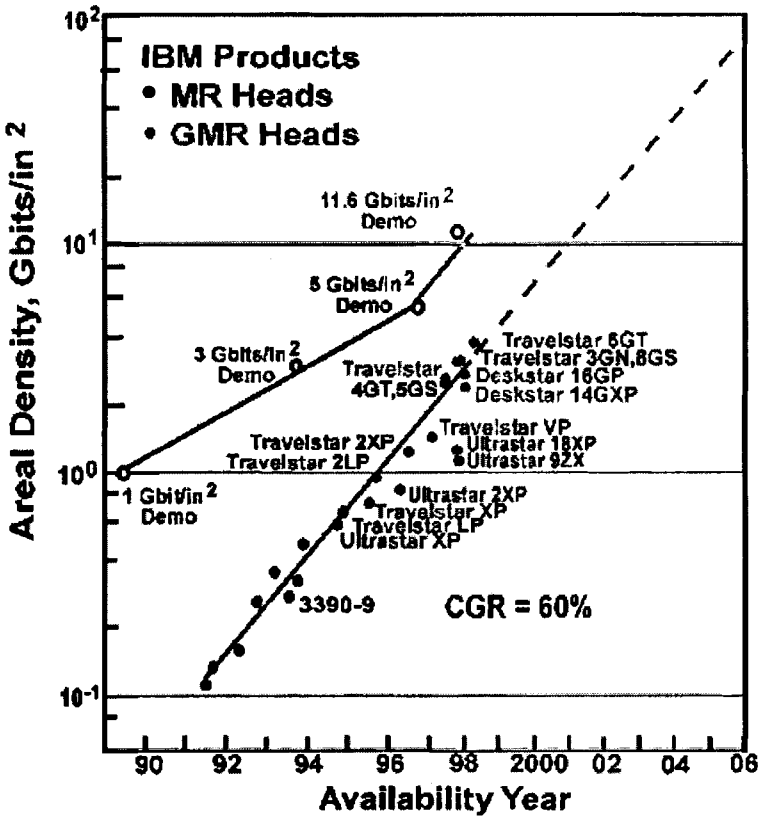

Figure 1.1: Areal density perspective of IBM HDD products

For manufacturing GMR structures, precise film deposition techniques are required to control film thickness and properties. GMR structures are typically multilayered stacks of thin films with the thickness of individual layers 100Å or less. Therefore, the thesis will

address thin film processing of rutile structures of ferromagnetic CrO_2 suitable for eventual GMR device development. Specifically, we will show how CrO_2/RuO_2 sandwich structures can be deposited by chemical vapor deposition.

1.2 Organization

The focus of this thesis is the stability of ultrathin metal dioxide (MO_2) rutile structures on single crystal TiO_2 substrates. The structures, with CrO_2 which is a ferromagnetic metal, are examined for potential in GMR device development. It starts by reviewing magnetoelectronics in Chapter 2, and discussing the mechanism of ferromagnetism and its applications in GMR. Chemical vapor deposition (CVD) is introduced in Chapter 3. We review CVD, its advantage and disadvantage in GMR materials synthesis, and explain about metal dioxide (MO_2) thin films with rutile structures and their application in industry. Chapter 4 introduces experimental procedures for CrO_2 deposition using CVD and discusses thin film characterization techniques including x-ray diffraction (XRD) and atomic force microscopy (AFM). The growth method for RuO_2 thin films deposited on several substrates is summarized in Chapter 5. Finally, the conclusions are discussed in Chapter 6.

CHAPTER 2

MAGNETOELECTRONICS

Electrons have both charge and spin. Traditional electronic devices have utilized only electronic charge. Continual trends toward minimization, low cost and high performance challenge traditional semiconductor-based electronics to give way to quantum mechanics-based electronics related to the use of electron's spins instead of electrons or holes. The field called magnetoelectronics is based on the study of spin-dependent electron transport between ferromagnetic layers and nonmagnetic or insulating layers. This chapter starts with a brief review of the giant magnetoresistance (GMR) effect exhibited by magnetic multilayers and moves to ferromagnetism.

2.1 Giant magneto-resistance

2.1.1. Overview

The magnetoresistance (MR) in a metal is the change of electrical resistance depending on the applied magnetic field. The discovery of this type of MR dates back to Lord Kelvin who noticed in 1856 that the electrical resistance of iron increased by 3.3% when subjected to a magnetic field. Typically, the electrical resistance of ferro-magnetic metal placed in a magnetic field increased by less than 5% at room temperature and by at most 30% at 4.2K.

In 1988, new types of structures, where the resistance change increases by greater

than 10% at room temperature, were discovered by Baibich *et al.* [6] Single crystalline (100) oriented Fe/Cr/Fe sandwiches and (100) oriented Fe/Cr multilayers exhibited much larger magnetoresistance than expected of individual Fe layers themselves. It is described as Giant because the resistance change is much larger effect than had ever been previously seen in metals. The synthesis techniques for these films are based on the vapor phase processes such as molecular beam epitaxy (MBE), chemical vapor deposition (CVD), sputter-deposition method, etc. To date, the largest GMR effect at room temperature is found in Co/Cu multilayers.[6] The interest in nanostructured metal multilayers with novel physical properties has greatly increased in recent years with the discovery of the giant magnetoresistance phenomenon.

2.1.2. GMR mechanisms

There are two types of multi-layer structures that exhibit GMR. First, the Ruderman-Kittel-Kasuya-Yosida (RKKY) interaction has been able to describe the origin of exchange coupling between ferromagnetic and non-magnetic layers.[8-10] The RKKY interaction explains that the exchange coupling results from the propagation of electrons between the ferromagnetic layers and non-magnetic spacer, which is determined by the oscillation period.[8] As proven by experiments, the period is affected by the spacer materials and its crystallographic orientation. The oscillatory exchange coupling is the coupling between the magnetic layers that oscillates in sign as a function of the spacer layer thickness. The RKKY exchange coupling requires lattice matching and band structure matching between ferromagnetic and non-magnetic layers. Therefore, some metal combinations are difficult to reconcile with a RKKY coupling mechanism

suggested by the oscillatory exchange coupling on the non-magnetic spacer separation.[9,10]

Another structure which exhibits GMR is a spin-dependent tunnel junction (SDT) where an electron flows through the junction perpendicular to the layers by tunneling from one ferromagnetic layer to the other through an insulating layer. The density of states available for electron tunneling change depending on whether the magnetizations of the ferromagnetic layers are in parallel or antiparallel. The electrical resistance of the tunnel junction alters as its magnetic state is changed.

GMR structure is composed of alternating ferromagnetic layers separated by non-magnetic spacer. GMR can exhibit large changes in electrical resistance when subjected to magnetic field.[11,12] When no external magnetic field is applied to the material, the electrons in top and bottom ferromagnetic layers have the opposite spin direction. If a small current is induced, some of the electrons in the top magnetic film will approach at the boundary with non-magnetic interlayer. If the non-magnetic interlayer have a good atomic lattice match to the magnetic film, electron will pass through the boundary with a low possibility of being scattered. When the electrons approach the bottom magnetic layer, they will have a high possibility of scattering because the electrons in bottom magnetic layer have all opposite spin direction. In this condition, the material has its highest resistance state. Consider the opposite case. If an external magnetic field is applied with certain strength, this makes magnetic moments of ferromagnetic layers parallel. If a current is induced through the material, some of the electrons in the top magnetic film can go through to the bottom magnetic layer without obstacle since all the electrons have the same spin directions. It creates the low resistance state in the material (Figure 2.1). When the ferromagnetic layers are antialigned, the spin-dependent

scattering is maximized, leading to highest state of resistance. The directions of magnetic moments result from applied external magnetic field.

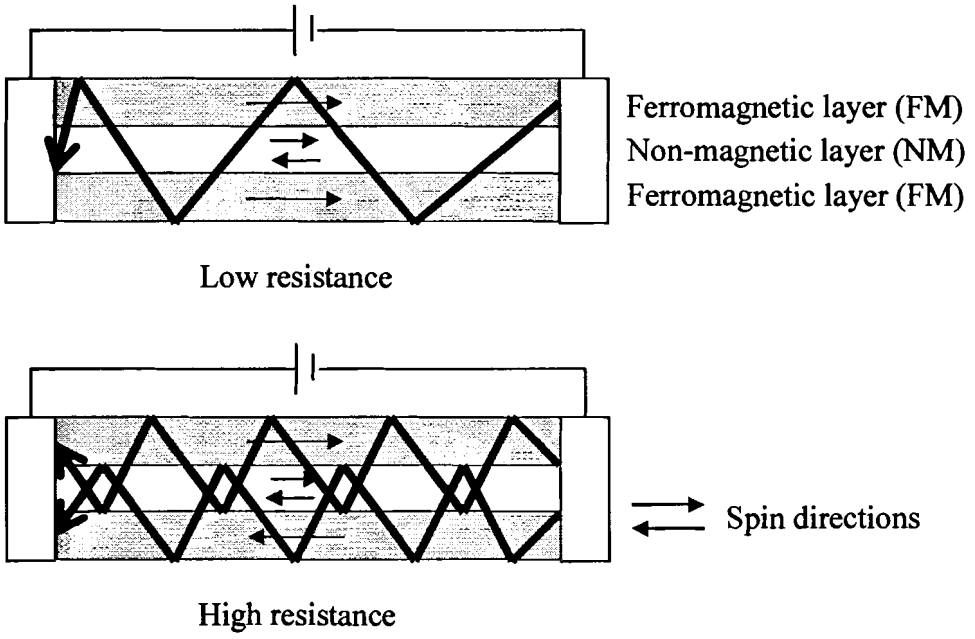

Figure 2.1: Schematic representations of electron transport in layered magnetic metal structure

In this thesis, CrO_2/RuO_2 sandwich structures like this will be fabricated at section 5; CrO_2 are used as a ferromagnetic layer (FM) and RuO_2 as a non-magnetic metal layer (NM).

2.1.3. Experimental observation of GMR

Figure 2.2 shows the resistance change ΔR/R vs magnetic field for two multilayers of Fe/Cr and Co/Cu.[6] In the figure, the resistance change is large at low magnetic field while small at high field. The resistance change depends on the change of spin directions of ferromagnetic Fe and Co layers with applied magnetic field. The resistance is high when the ferromagnetic layers are aligned antiparallel to each other compared with parallel alignment.

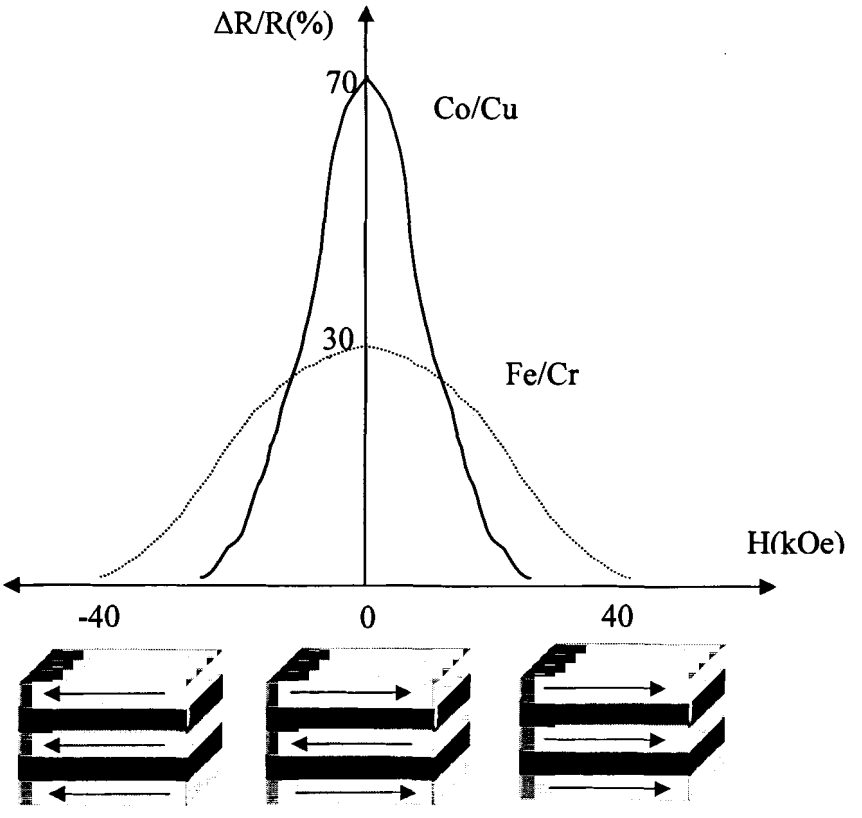

Figure 2.2: Room temperature resistance vs magnetic field for Co/Cu and Fe/Cr multilayers

For a small applied magnetic field, ferromagnetic layers are aligned antiparallel each other. This is a consequence of an antiferromagnetic interlayer coupling through Cr or Cu layers. When ferromagnetic Co layers are aligned antiparallel, a large GMR value is expected. For strong ferromagnetic coupling of Co layers, the relative magnetic alignment of the Co layers is not affected by applied magnetic field, and consequently there is no GMR effect.

2.2 Ferromagnetic materials

Ferromagnetism results from an imbalance of spin populations (spin up, spin down) at the Fermi level of Fe, Ni, Co and their alloys. Figure 2.3 shows the comparison of the density of electron states between a normal metal (Cu) and a ferromagnetic material (Co).[11,12]

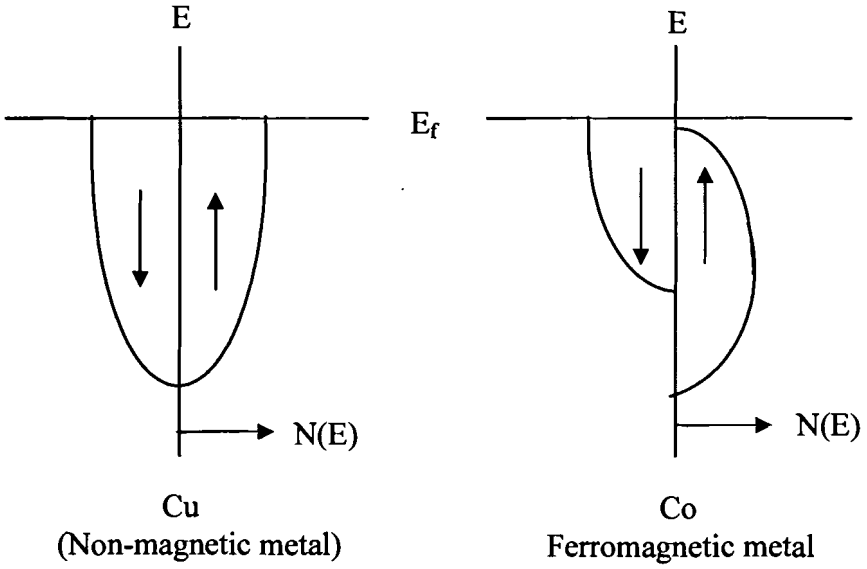

Figure 2.3: A schematic representation of density of electronic states in Cu and Co

The non-magnetic metal has the same number of up-spin and down-spin electrons at the Fermi level. Therefore, there is no net magnetic moment, and the electrons at the top of the filled state, called the Fermi level, are unpolarized. In the case of ferromagnetic materials, such as cobalt, there is a spin imbalance. This spin inequality produces a net magnetic moment in a material. The unpaired electrons can be easily lined up with each other toward the direction of applied magnetic field due to exchange interactions. Also, ferromagnetic materials have a strong induction interaction with applied magnetic fields and can remain magnetized permanently in the absence of an external magnetic field below a certain temperature, called the Curie temperature. Another important intrinsic property in ferromagnetic materials is spin polarization (P), which is defined in terms of the number of carriers n that have spin up ($n\uparrow$) or spin down($n\downarrow$), as $P = (n\uparrow - n\downarrow) / (n\uparrow + n\downarrow)$. The materials for which P is less than unity are referred to as partially polarized, spin polarization was determined to be 44% for iron, 34% for cobalt and 11% for nickel.[11,12]

The performance of a spin-dependent tunnel junction (SDT) is directly related to the spin-polarization in the magnetic layers as shown in Figure 2.4. Clearly, very exciting device possibilities become available when using materials with $P \rightarrow 100\%$. As $P \rightarrow 100\%$, true on-off switching is available with the device impedance approaching infinity in the off state. Switches such as these could replace transistors in computer chips resulting in non-volatile logic and new approaches to computing.

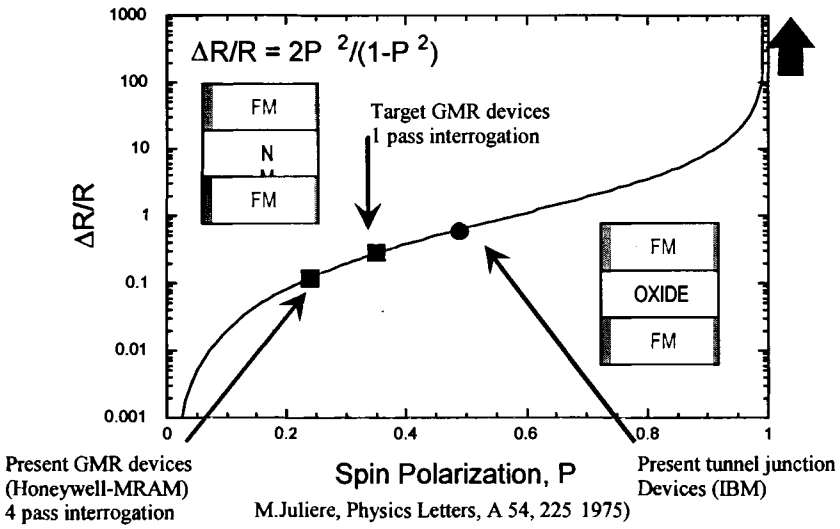

Figure 2.4: Technological impact of nano scale devices fabricated with highly spin-polarized materials like CrO_2. The change in resistance measured with an applied magnetic field is plotted as a function of spin-polarization of the ferromagnetic (FM) material.

It is clearly desirable to develop GMR structures and devices with materials having $P \rightarrow 100\%$. The device performance is directly related to the availability and quality of highly spin-polarized materials. Unfortunately, there are a limited number of candidates, including CrO_2, Ni(Pt)MnSb, and $La_{1-x}Ca_xMnO_3$. These materials all present unique synthesis challenges to the crystal grower that are not encountered when depositing thin layers of metals. All are compounds requiring strict attention to stoichiometry in the case of NiMnSb and $La_{1-x}Ca_xMnO_3$, and cationic valence state in the case of the metastable CrO_2. Of these compounds, CrO_2 is structurally the simplest, crystallizing in the rutile structure (tetragonal). In addition, its theoretically predicted half-metallic nature has been confirmed experimentally. Highly spin-polarized thin CrO_2 films have been prepared.

2.2.1 Domain structure

Within the grain structure of a ferromagnetic material, there are regions composed of different magnetic alignment directions.[15,16] These regions are called Domains. Without an applied magnetic field, individual domains have a random orientation. Therefore, the overall net magnetic moment in the material is zero. The interface, called Block walls, separates the domains. With an applied magnetic field, the directions of magnetic moments change gradually in the block wall (Fig 2.5), which is influenced from direction of one domain to that of the next domain. Each domain has oriented along its crystallographic orientation. Usually a domain is much smaller than a grain size. When exposed to an external magnetic field, domains that are lined up with an applied field grow continually at the expense of unaligned domains. To grow a domain, the block walls must move. At first, it is difficult for a domain to grow. With continual increases in the strength of the magnetic field, favorably oriented domains grow more easily. Eventually, unfavorably oriented domains disappear. The saturation magnetization, where all of domains are properly oriented, is the greatest amount of magnetization.

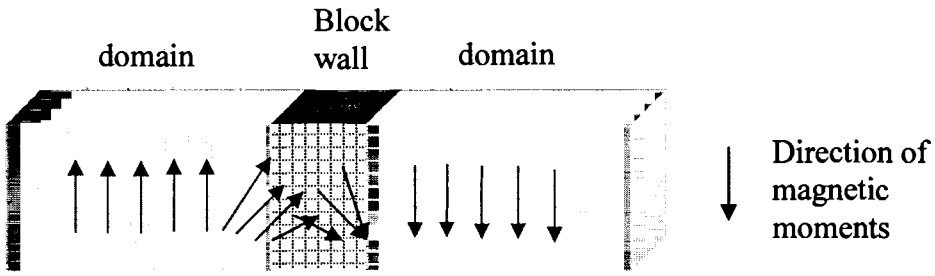

Figure 2.5: The magnetic moments change across the block wall between domains

2.2.2 Hysteresis loop

Figure 2.6 illustrates an example hysteresis curve for ferromagnetic materials. Initially, the ferromagnetic material is unmagnetized (point a). As the external magnetic field (*H*) is increased, the induced magnetization (M) also increases. The induced magnetization eventually saturates (point b). The curve between points "a" and "b" is called the magnetization curve. Now, if the external field is reduced, the induced magnetization also is reduced, but it does not follow the original curve. Instead, the material retains a certain permanent magnetization called the remnant magnetization Mr(infinity) (point c). If the external field is reduced more in other direction, the remnant magnetization will eventually be removed (point d). The external field for which the remnant magnetization goes to zero is termed the coercivity, Hc. As the external field continues to reverse, permanent magnetization of the opposite sign is created in the magnet. A similar curve is traced for the negative direction with saturation

(point e), remnant magnetization (point f) and coercivity (point g). The hysteresis curve then retraces points b-e as the field cycles.

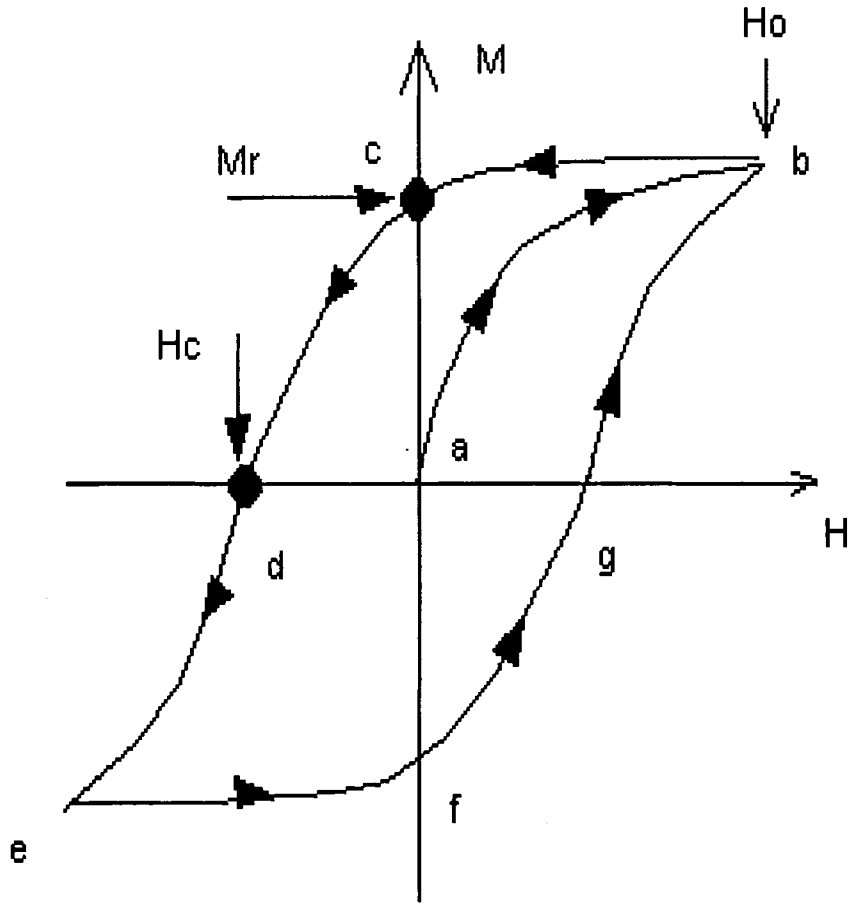

Figure 2.6: Hysteresis curve for ferromagnetic material

CHAPTER 3

EXPERIMENT BACKGROUND

3.1 Chemical vapor deposition

The deposition of thin films on various substrates is a key element of manufacturing of microelectronic and optic devices. Deposited films must have a high purity and uniformity. Chemical vapor deposition (CVD) is commonly used in fabrication techniques because CVD has great advantages to depositing thin films. In this process, where one or more volatile inorganic, metal-organic, or organometallic precursors are transported in the vapor phase, with carrier gases, to the reactor where they decompose on a heated substrate to form a nonvolatile solid film, followed by the elimination of volatile byproducts (Fig 3.1).[17-19] Using CVD, a variety of thin films possessing high purity and desirable properties can be produced on various substrates. The control of reaction chemistry and deposition conditions can tailor chemical composition and physical properties of thin films. Furthermore, the capability of controllably creating films of widely varying stoichiometry makes CVD unique among deposition techniques. Other advantages include low cost of CVD equipment, low operating expenses, and compatibility with other processing steps.

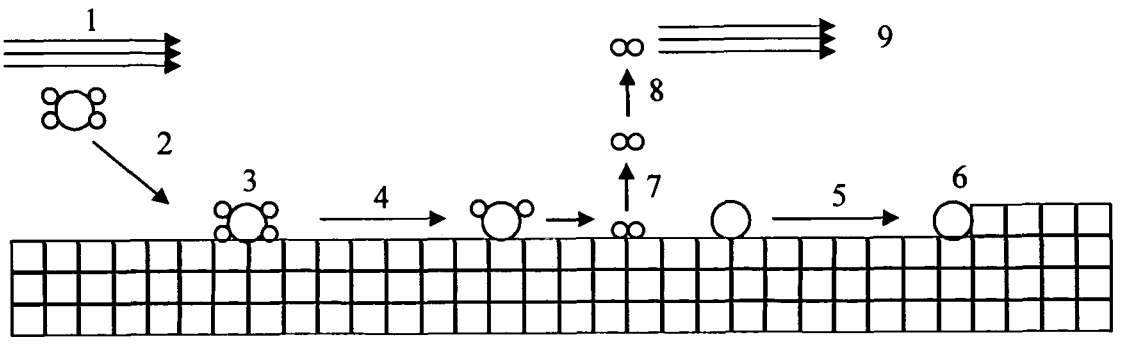

Figure 3.1: Illustration showing the fundamental steps involved in CVD

As illustrated in Figure 3.1, CVD is a heterogeneous reaction including the following steps:

Arrival

1. Bulk transport of reactant into the process volume
2. Gaseous diffusion of reactant to the surface
3. Adsorption of reactants onto the surface

Surface reaction

4. Surface reaction (reaction can also take place in the gas volume immediately over the surface)
5. Surface diffusion
6. Crystal lattice incorporation

Removal of reactant by-products

7. Reaction by-product desorption
8. Gaseous transport of by-product
9. Bulk transport of by-product out of process volume

The rate of chemical vapor deposition is primarily determined by one of following

process steps.

- The rate of arrival of reactants
- The surface reaction rate
- The rate of removal of by-products

Inert carrier gases such as Ar and N_2 are used to increase rate of transport of solid or liquid precursors to the reactor.[19] However, other reactive gases such as H_2, NH_3, and O_2 are also used to participate in the chemistry of film deposition by acting as reducing or oxidizing agents.

3.1.1 Growth kinetics

Both gas-phase transport rates and surface reaction rates are important in CVD and one of them can be rate-limiting. Figure 3.2 shows a simple model of the film growth process.[17]

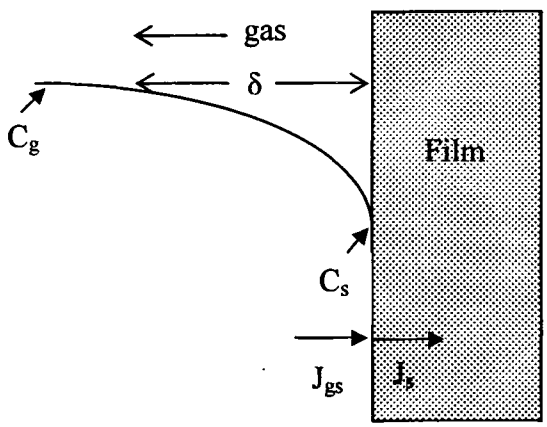

Figure 3.2: Model of growth process

As, reactants are consumed, a drop in concentration of the reactant from C_g in the bulk of gas to C_s at the interface occurs. The corresponding mass flux is

$$J_{gs} = h_g (C_g - C_s) \tag{3.1}$$

where h_g is the gas-phase mass-transfer coefficient.

The flux consumed by the reaction taking place at the surface of the growing film is

$$J_s = k_s C_s \tag{3.2}$$

where k_s is rate constant for surface reaction.

In the steady state, $J_{gs} = J_s$

$$C_s = C_g / (1 + k_s/h_g) \tag{3.3}$$

If $k_s >> h_g$, this formula predicts that surface concentration drops to zero, indicating mass-transfer control. In this case, low gas transfer through the boundary layer limits the rapid surface reaction. On the other hand, if $h_g >> k_s$, C_s approaches C_g. Therefore the surface reaction limits the growth rate.

The film growth rate is given by

$$G = J_s / N_0 = (k_s h_g / k_s + h_g) (C_g / N_0) \tag{3.4}$$

where N_0 is the atomic density or the number of atoms incorporated into the film per volume. The temperature dependency of G is related to the properties of k_s and h_g. Here k_s is expressed by

$$k_s = K_s^0 \exp(-E / RT) \tag{3.5}$$

where E is the activation energy involved. h_g is related D / δ. D depends on the pressure and temperature as $\sim T^{3/2} / P$. Since both D and δ are weakly dependent on temperature, h_g is relatively insensitive to variations in temperature. At low temperature, film growth is limited by the surface reaction rate; i.e., $G = k_s C_g / N_0$, since the rate of arrival of

reactant is faster than the surface reaction rate.

At high temperature, the mass transfer or diffusion rate limits the growth rate; i.e., $G = h_g C_g / N_0$, since the overall surface reaction rate usually increases more rapidly than the overall mass transport rate. Each growth rate can be described by a diffusion controlled regime or a surface reaction controlled regime, as shown in Figure 3.3.[19]

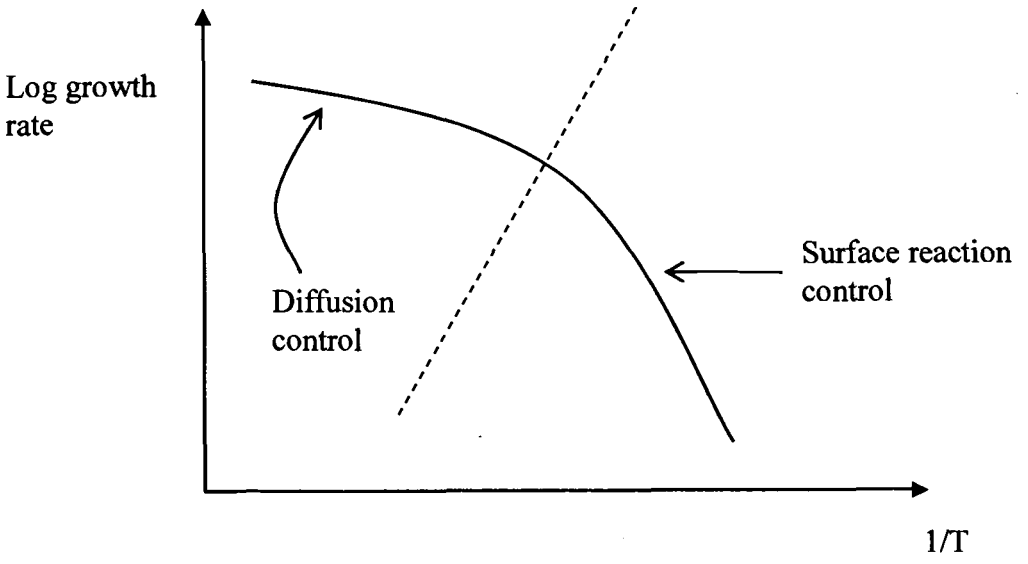

Figure 3.3: Typical overall reaction rate for CVD reactors vs. reciprocal temperature

3.1.2. CVD reactors

Chemical vapor deposition reactors are often described by the method used in heating the substrate. In a hot-wall reactor, the substrate, as well as the reactor walls, is heated via radiant heating (Figure 3.4).[18]

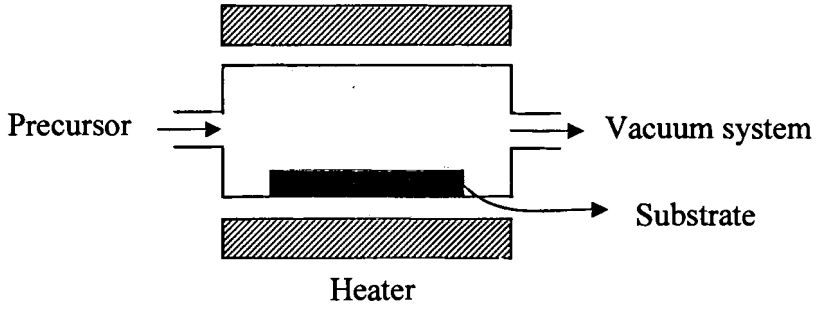

Figure 3.4: Hot-wall CVD reactor

Hot-wall CVD reactors often can process many substrates at once for high throughput. This is because heating occurs on the reactor wall as well as the substrate and film. Deposition takes place on both the substrate and reactor walls; this gives a wider deposition zone allowing simultaneous deposition on multiple substrates. In a cold-wall reactor only the substrate is heated and reactions take place on the substrate surface. The cold-wall reactor has the disadvantage of a narrow deposition zone and a low throughput (number of deposited films/time unit) (Figure 3.5).

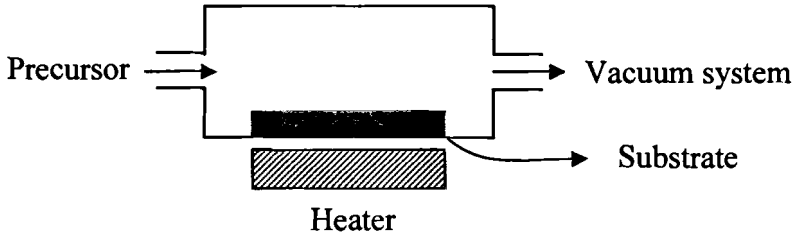

Figure 3.5: Cold-wall CVD reactor

3.2 Thin film structural development

The film formation usually follows one of three basic growth modes: (1) island (or Volmer-Weber), (2) layer (or Frank-van der Merwe), or (3) Stranski-Krastanov, which are shown in Figure 3.6.

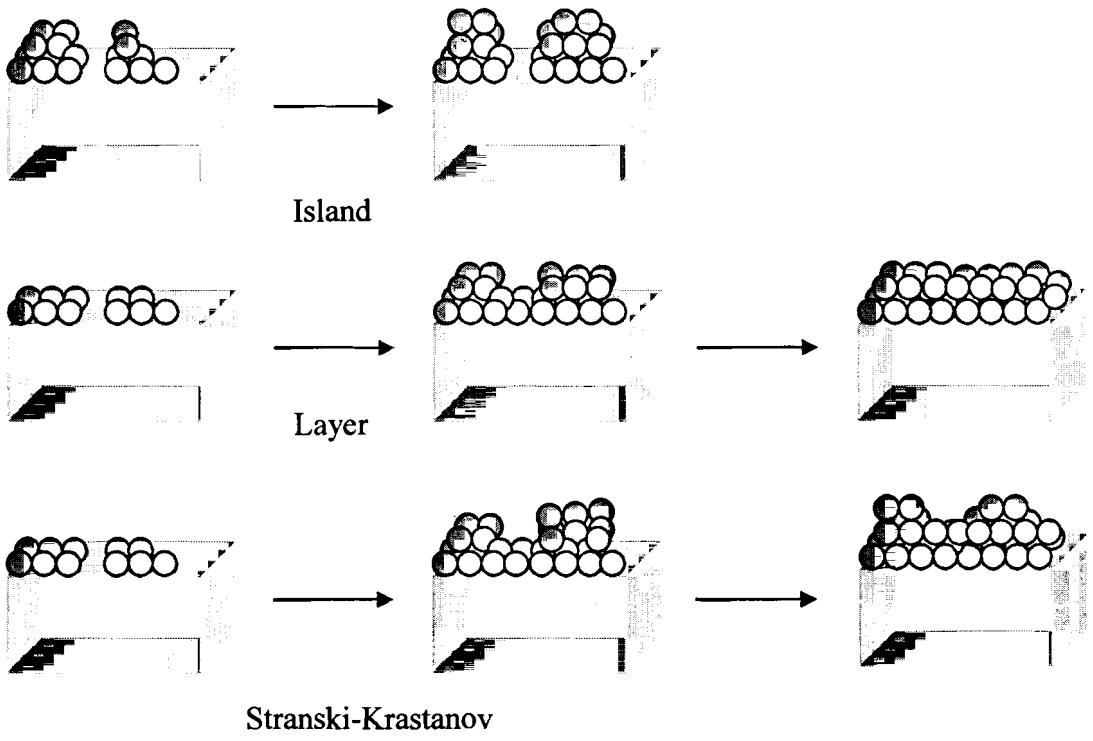

Figure 3.6: Basic modes of thin-film growth

Island growth occurs when small clusters nucleate on the substrate and grow in three-dimensions. This island growth occurs when atoms are bound more strongly to each other than to the substrate. Many metal compounds on insulators display this growth mode. The opposite growth mode is observed during layer growth. Small clusters nucleate on

the substrate in two dimensions resulting in the formation of planar sheets. In this growth mode, atoms are more strongly bound to the substrate than to each other. The example of this growth mode is the single crystal epitaxial growth of semiconductor films. The Stranski-Krastanov growth mode is the island plus layer growth mode. In this growth mode, after forming one or more monolayers by layer growth, the growth mode switches to island growth.

Although the mechanism for the change from two- to three-dimensional growth is not completely understood, some possible factors can be considered. For example, from the film-substrate lattice mismatch, strain energy accumulates in the growing film. When released, the high energy at the deposit-intermediate layer interface may start island formation. This growth mode is general and can be observed in metal-metal and metal-semiconductor systems.

In Figure 3.7, the illustration of film classification on basis of orientation and perfection is shown. The substrate shown in the figure is considered to be a single crystal substrate. In Figure 3.7 panel I, the film is random polycrystalline. In panel II, one-dimensional orientation (along the film deposition directions) is observed in the film. There is no crystalline orientation within the plane of growth in association with the substrate. There is also modest misalignment along the growth direction. In panel II, high angle grain boundaries are observed.

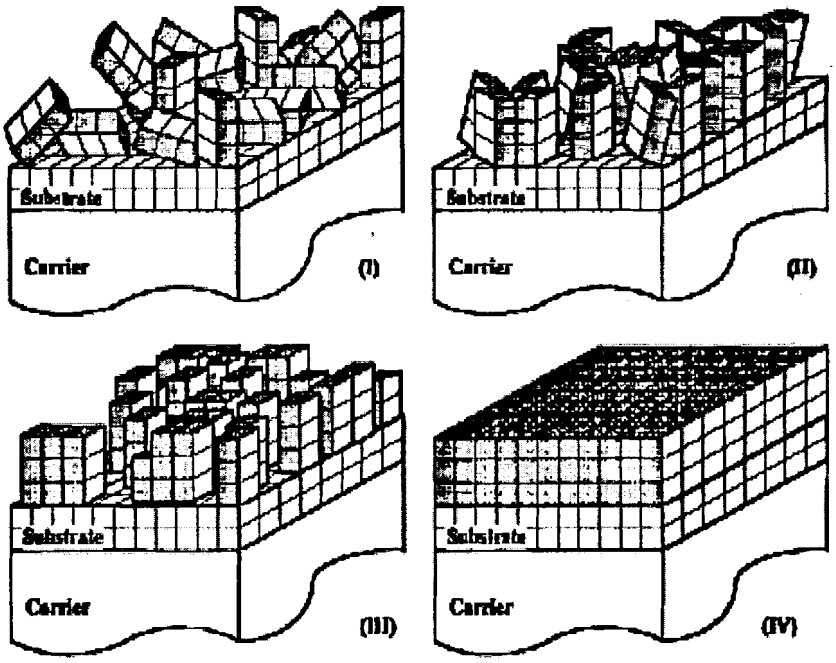

Figure 3.7: Film classification terminology, (I) random polycrystalline, (II) polycrystalline, (III) polycrystalline with epitaxial growth, and (IV) single crystalline

The film in panel III is still polycrystalline with epitaxial orientation. Although the individual grains are very well oriented in both the c and the a, b directions, they are not connected in the plane. This film contains various defects, such as cracks, voids, tunnels, growth twins, antiphase boundaries, ferroic twins, steps, and phase or composition deviation. Steps (as shifted fractions of the structural repeat unit) in the c and the a or b directions due to nucleation at different contact sections of the unit cell are shown in figure (III). Figure (IV) shows ideal single crystal film with epitaxial orientation. This film is continuous throughout the large areas. A polycrystalline film (III) has considerably higher tolerance for lattice mismatch than a single crystal film (IV) due to the buildup of mismatch over several unit cells.

3.3 Metal dioxide thin film with rutile-related structures

Rutile structures have the general formula AX_2, where A represents transition metal ions and X represents oxide, fluoride, nitride or iodide. Rutile oxide structures like MO_2 have received considerable attention when compared with MF_2 or MI_2 . The M expresses several metal ions with a positive 4 charge. Oxides, due to great variety and complexity of their structure, form numerous materials that exhibit a wealth of interesting and useful properties that can be exploited for a variety of technological applications. Many of the oxide materials have been studied in the form of thin films due to their various applications. Generally, several transition metals such as lead (Pb), titanium(Ti), tin (Sn), manganese (Mn), vanadium (V) and ruthenium (Ru) are included in this rutile oxide group. The rutile group compounds have tetragonal unit cell with a = b c. This structure is composed of parallel chains of octahedrons, which means each metal ion is surrounded by six oxygen atoms and each oxygen is surrounded by equilateral triangle of metal atoms. Therefore, the rutile structure is characterized by having a cation coordination number of 6. Figure 3.8 shows the rutile structure. As shown in panel (b), rutile structure can be visualized as chains of edge-sharing octahedral in c-direction. These chains share corners with each other in the a and b-directions, as shown in panel (c). As a result, metal-metal interactions are stronger in the c-direction. These interactions, particularly for transition metals with partially filled d-orbitals, results in a wide variety of electronic and magnetic properties for materials crystallizing in the rutile structure. In VO_2, V ions form alternating short and long pairs in the c-direction at room temperature. At 68°C distance between V ions becomes uniform (rutile structure) and the material changes from a semiconductor to a metal.

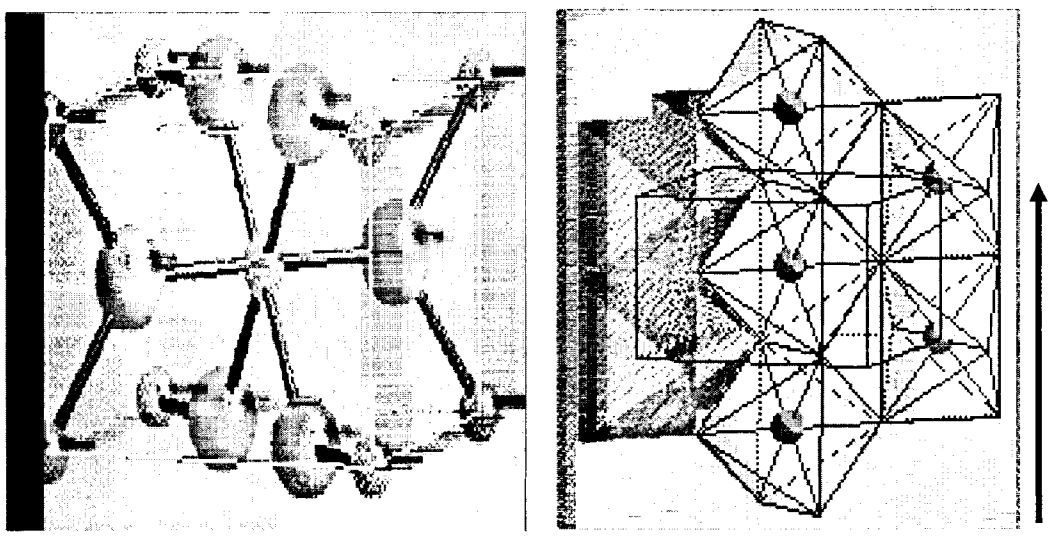

(a) 6-coordinate metal cation (b) Edge-sharing octahedral in c-direction

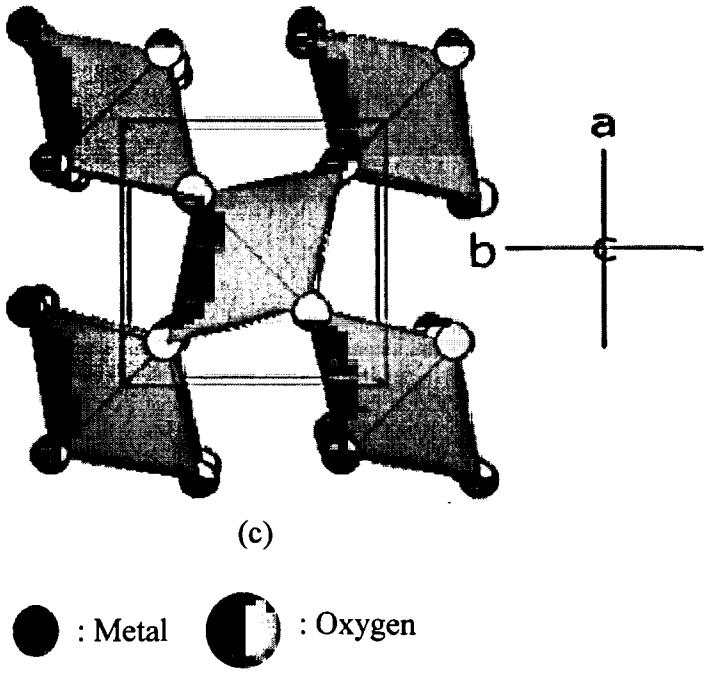

Figure 3.8: The rutile structure

Some compounds with rutile structure (oxides of some tetravalent metal ions) are listed in Table 3.1.[20]

Table 3.1: The crystal data for selected MO_2 compounds with rutile-related structure

	a(Å)	c(Å)	Electron config.	Average Me-O distance (Å)	Closest Me-Me distance (Å)
SiO_2	4.176	2.666	$2p^6$	1.768	2.67
TiO_2	4.5937	2.9581	$3d^0$	1.959	2.96
MnO_2	4.398	2.8738	$3d^3$	1.90	2.87
CrO_2	4.41	2.91	$3d^2$	1.905	2.92
GeO_2	4.395	2.859	$3d^{10}$	1.90	2.86
IrO_2	4.49	3.14	$5d^5$	1.99	3.15
MoO_2	4.86	2.79	$4d^2$	2.011	2.51
NbO_2	4.77	2.96	$4d^1$	2.048	2.80
OsO_2	4.51	3.19	$5d^4$	1.99	3.18
PbO_2	4.946	3.379	$5d^{10}$	2.135	3.38
RuO_2	4.51	3.11	$4d^4$	1.971	3.11
SnO_2	4.7373	3.1864	$4d^{10}$	2.053	3.19
TaO_2	4.709	3.065	$5d^1$	2.02	3.06
WO_2	4.86	2.77	$5d^2$	2.01	2.49
VO_2 (tetra)	4.552	2.846	$3d^1$		2.85
VO_2(mon)	5.743	5.375	$3d^1$	1.937	2.62
RhO_2	4.4862	3.0884	$4d^5$	1.98	3.09

Most metallic oxides with the rutile structure have very interesting properties and a variety of industrial applications. Three compounds with rutile structure are described in the next section.

3.3.1. Titanium dioxide (TiO_2)

TiO_2 crystallizes in three different structures: rutile, anatase and brookite structure. Only rutile and anatase structure are important technically or commercially. The rutile structure has a density of 4.2g/cc, while anatase structure has a density of 3.9g/cc. The rutile is more closely packed than anatase. The anatase-to-rutile TiO_2 transition occurs after heating to 800°C. Rutile TiO_2 thin films are used for coatings because of their

desirable properties, such as good transmission in the visible and near infrared regions, good adhesion, and high stability against mechanical abrasion, chemical attack, and high temperature. Therefore, rutile TiO_2 thin films are used in single-layer or multilayer optical coatings.

3.3.2. Chromium dioxide (CrO_2)

Chromium dioxide (CrO_2) is a ferromagnetic oxide that has been widely used in recording media. Bulk CrO_2 has a rutile structure with a tetragonal unit cell (a=b=4.421Å, c=2.916Å) with 200 μΩ-cm room temperature resistivity. CrO_2 has a Curie temperature of 395K.

Magnetic materials exhibiting high spin polarization are being studied actively for magnetoelectronic devices. To date, the materials that are only partially polarized (such as Fe, Co and Ni, which have a spin polarization P of 40 to 50%)[11,12] are being used for industry. Efforts to find materials with complete spin-polarization are important. Some materials, such as CrO_2, $La_{1-x}Ca_xMnO_3$ and NiMnSb (Heusler alloys), have been predicted theoretically to have 100% spin-polarization. Based on the theoretical band structure calculation, CrO_2 is considered to be a half metal with almost complete spin polarization;[21-29] the majority spin (up-spin) electrons have metallic band structure while the minority spin (down-spin) electrons have a semiconductorlike band gap at Fermi level. Thus CrO_2 appears to be anctive candidate for the fabrication of magnetoresistance devices. Since CrO_2 is metastable, the fabrication of thin films of CrO_2 is often difficult, requiring epitaxial growth on appropriate substrates. Furthermore, CrO_2 exists in many oxides forms such as CrO_2, CrO_3, Cr_2O_5, and Cr_2O_3,[21] where Cr_2O_3 is the most stable

form. CrO_2 has been shown to irreversibly change to Cr_2O_3 at temperature below 320 and above 380 °C. Despite many difficulties, there have been continual efforts to deposit CrO_2 thin films.

3.3.3. Ruthenium dioxide (RuO_2)

Another thin film, studied in my thesis, is ruthenium dioxide (RuO_2). Recently highly conductive RuO_2 thin films have attracted considerable interest, particularly for applications in ultralarge scale integrated (ULSI) circuits.[42-49] RuO_2, which has a resistivity of as low as 40 μΩ-cm and a high resistance to chemical attack and good thermodynamic stability, has been used as an electrode for high dielectric (Ba,Sr)TiO_3 thin films. We are interested in RuO_2 as the non-magnetic layer in GMR structures because it has the same structure as CrO_2 and has similar lattice constant. RuO_2 has a rutile structure with lattice constants of a = b = 4.499 , c = 0.107 . Deposition of RuO_2 thin films is much less complicated because RuO_2 is the most stable oxide stoichiometry and is not dependent on the deposition temperature.

CHAPTER 4

PHASE-SELECTIVE CHEMICAL VAPOR DEPOSITION OF CHROMIUM OXIDES FROM CHROMYL CHLORIDE

4.1 Introduction

Recently the technology based on the spin polarization has been attracting significant interest. With increasing demands for much smaller and efficient devices, which cannot be realized with semiconductor based devices, a new field known as magnetoelectronics is emerging. The primary idea for this technology comes from ferromagnetic materials. Among several ferromagnetic materials, chromium dioxide (CrO_2) is the best candidate for magnetoelectronics devices because it is considered to be 100% spin polarized at the Fermi level and can be fabricated relatively easily due to its simple stoichiometry. Therefore, as a first step, an efficient and controlled CVD process for CrO_2 films deposition on TiO_2 substrates using CrO_2Cl_2 precursor is described. Second, the concept of multifuctionallity on a computer chip requires materials with unique properties to be fabricated onto semiconductor wafers, particularly Si.The possibility of CrO_2 film fabrication on Si substrates is also studied.

4.2 Experimental technique for CrO_2 thin film deposition

Chromium dioxide films have been grown on various single crystal substrates by chemical vapor deposition using several precursors, such as CrO_3 or CrO_2Cl_2. Mostly, thin film growth efforts have involved CrO_3 as a precursor.[22-29] Because of the properties

of CrO_3, a solid that sublimes at ~260°C and also partially decomposes, control of thin film properties is difficult. For CrO_2 film growth using CrO_3 as a precursor, a two-zone furnace is used: one zone to sublime the precursor and a second zone to completely decompose the precursor on the substrate. On the other hand, thin film fabrication using CrO_2Cl_2 as a precursor allows the use of state-of-the-art equipment: this equipments include precursor bubbler, automated valves, a pressure controller, mass flow controllers, and precursor sensors to deliver precise amount of precursors into reactor. Using this sophisticated precursor delivering equipment, CrO_2 thin film growth on TiO_2 substrates is more controlled. Therefore we chose to use CrO_2Cl_2 as a precursor for CrO_2 film growth on the TiO_2 substrate. This precursor is a liquid with a room temperature pressure of 24 Torr; this is similar to water. The melting point of -96.5°C and boiling point of 117°C make this precursor appropriate for our experiment. More cautious handling of CrO_2Cl_2 is needed due to its moisture sensitivity.

In our experiment, CrO_2Cl_2 was delivered to a bubbler and held at 2 to 3 °C for all experiments. High purity Ar gas was used as a carrier gas. The flow rate of Ar gas into the reactor was set between 20 and 200 sccm. The temperature of the reactor was held between 320 and 400 °C, and the substrate was placed at different positions. The experiments lasted for 1 to 2 hours. TiO_2 Substrates were cleaned in acetone, methanol, isopropanol, and a 25% HF solution, and then mounted in a hot wall CVD reactor. The thin film growth apparatus is shown in Figure 4-1. The reactor itself is a quartz tube with an inner diameter of 6.2cm, and the tube is mounted horizontally inside a furnace. To avoid turbulence of the reaction gas, substrates are laid on an aluminum plate layer in the reactor. To collect by-product Cl_2 and Ar gas, a small collector with water was used.

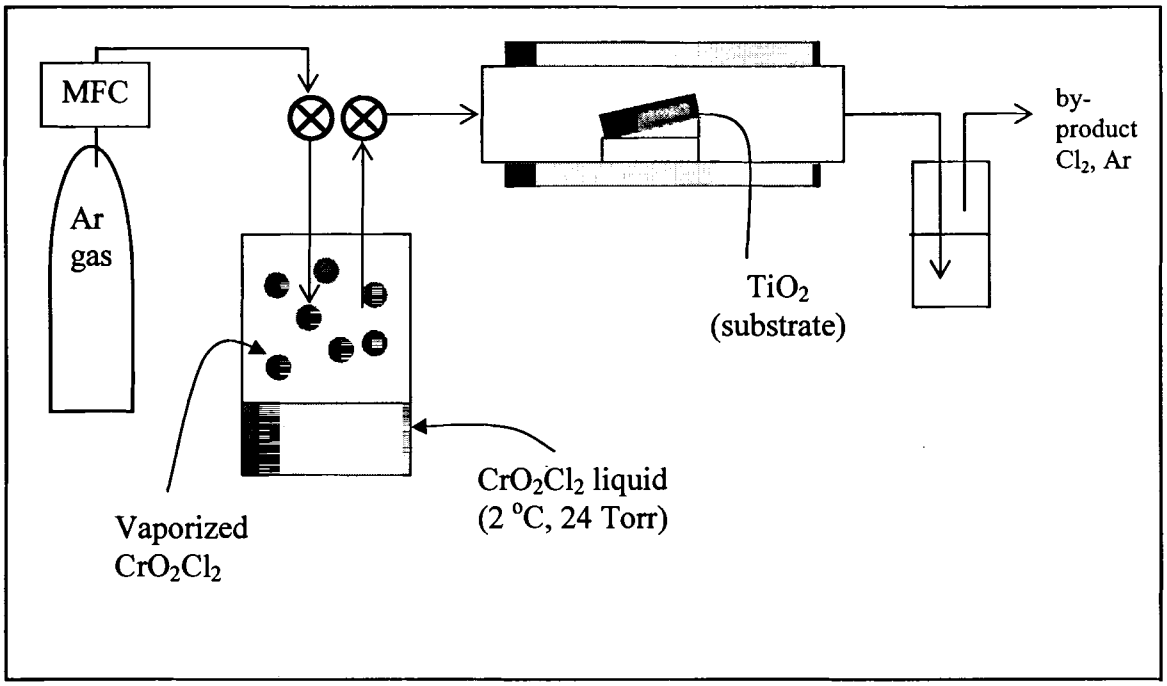

Figure 4.1: The apparatus for CrO_2 film growth

The furnace temperature varies along the reactor length. Figure 4.2 shows the temperature distribution of the reactor tube wall vs. distance. To determine the temperature profile, the furnace temperature was set at 350 and 400 °C and a thermocouple was positioned at various locations along the reactor. At a distance of 10 to 12 inch from the reactor entrance, the set point temperature was obtained.

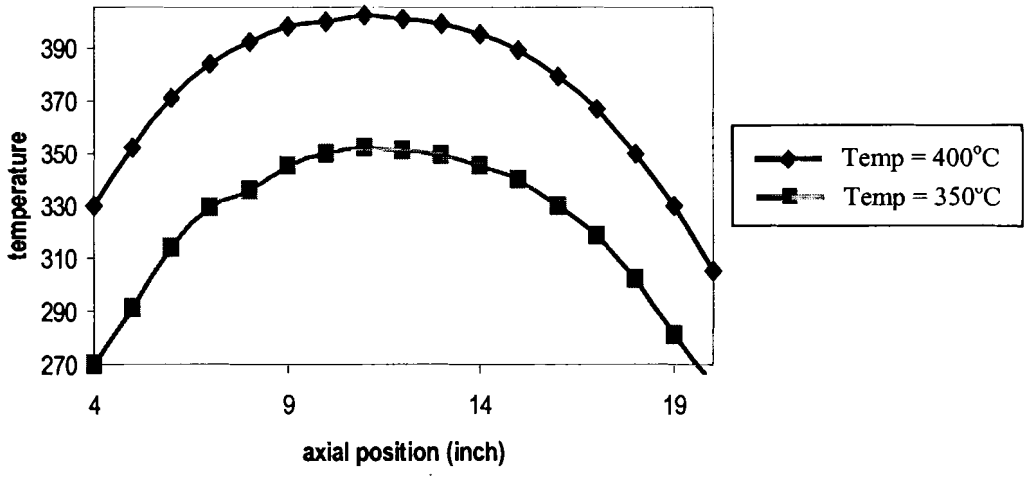

Figure 4.2: The temperature distribution of reactor tube wall

4.3. X-ray diffraction

X-ray diffraction is a very useful analytical technique for identification and quantitative determination of the various crystalline compounds that are present in solid materials and powders. X-rays are electromagnetic radiation with typical photon energies in the range of 100 eV - 100 keV.[39] For diffraction applications, only short wavelength x-rays in the range of a few angstroms to 0.1 angstrom (1 keV - 120 keV) are used. Because the wavelength of x-rays is comparable to the size of atoms, they are ideally suitable for exploring the structural arrangement of atoms and molecules in a wide range of materials. X-rays are produced generally by either x-ray tubes or synchrotron radiation. In an x-ray tube, which is the primary x-ray source used in laboratory x-ray instruments, x-rays are generated when a focused electron beam accelerated across a high voltage field bombards a stationary or rotating solid target. As electrons interact with atoms in the target and slow down, a continuous spectrum of x-rays are emitted, which

are termed as Bremsstrahlung radiation. The high energy electrons also eject inner shell electrons in atoms through the ionization process. When a free electron fills the shell, an x-ray photon with energy of the target material is emitted. Common targets used in x-ray tubes include Cu and Mo, which emit 8 keV and 14 keV x-rays with corresponding wavelengths of 1.54 Å and 0.8 Å, respectively. Figure 4.3 shows schematically x-ray diffraction facility.

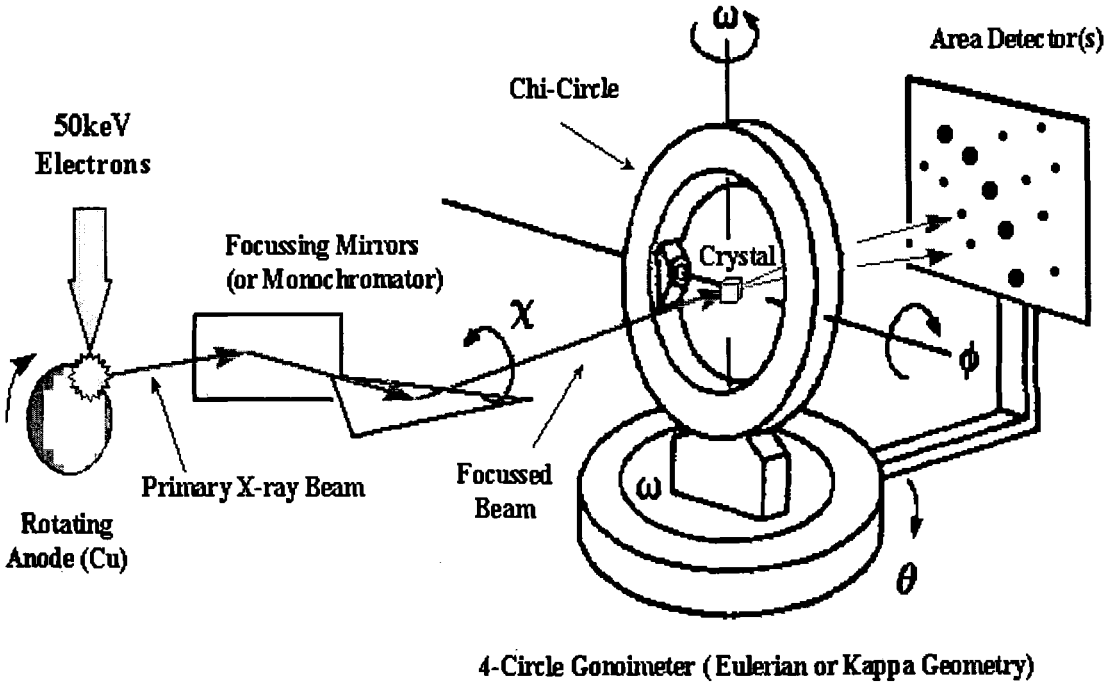

Figure 4.3: X-ray diffraction facility

X-rays primarily interact with electrons in atoms. When x-ray photons collide with electrons, some photons from the incident beam are deflected away from the direction where they originally travel. If the wavelength of these scattered x-rays did not change (meaning that x-ray photons did not lose any energy), only momentum has been transferred in the scattering process. These are the x-rays that we measure in diffraction

experiments, as the scattered x-rays carry information about the electron distribution in materials. X-ray diffraction can be explained by the "reflection" of an x-ray beam from a stack of parallel equidistant atomic planes. At each atomic plane, a small portion of the beam can be considered to be reflected. If those reflected beams, which are not absorbed through a crystal, emerge from the crystal in such a way that they do not cancel each other by interference, a diffracted beam can be observed. The condition where the reflected beams interfere positively (reinforce) to give a strong diffracted beam is given by Bragg's law.

$$\text{Bragg's law} : n\lambda = 2d\sin\theta \tag{4.1}$$

Where n is an integral number describing the order of reflection, λ is the wavelength of the x-rays, d is the spacing between the lattice planes and θ is the Bragg angle where a maximum in the diffracted intensity occurs. At other angles there is little or no diffracted intensity, because of destructive interference.

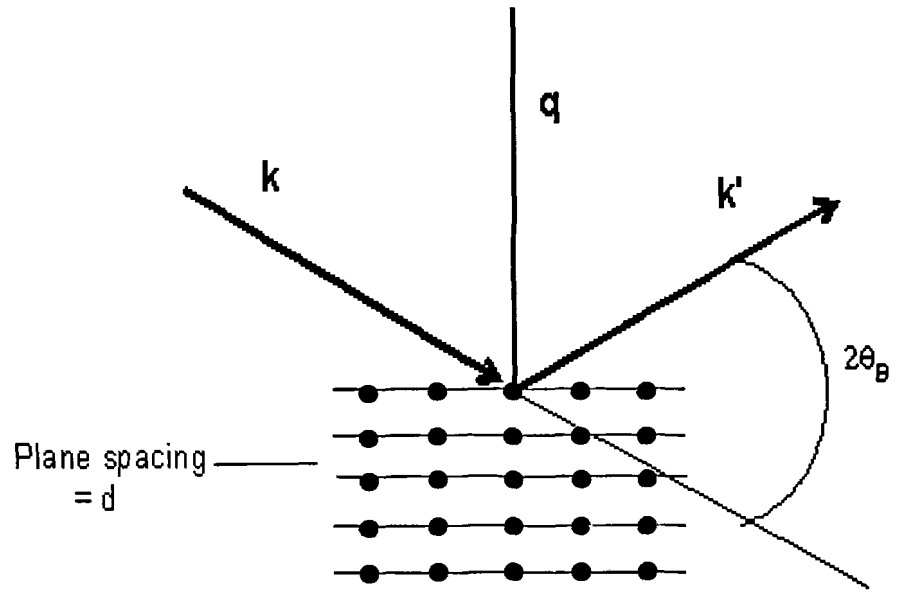

Figure 4.4: X-ray diffraction

Associated with the diffraction from this periodicity, there is a scattering vector, **q** , defined in terms of the initial (**k**) and final (**k'**) x-ray wavevectors as **q** = **k'** - **k**, whose magnitude is therefore

$$q = 4\pi \frac{\sin \theta_B}{\lambda} \tag{4.2}$$

By definition, **q** is always parallel to the direction of the periodicity that caused the diffraction.

There are two types of x-ray scans used in this thesis. These are shown schematically in Figure 4.5. For a θ /2θ scan (Figure 4.5a), **q** is at some angle $\eta = 90 - \chi$, typically 0, to the substrate normal. The motion of sample and detector in this case keeps the direction

of **q** fixed relative to the sample, and only the length of **q** changes as in above equation. With this scan, different periodicities along a certain direction are sampled.

In a Φ scan (figure 4.5b), **q** is set to some angle $\eta = 90 - \chi$ with respect to the substrate normal and 2θ is set to a particular diffraction condition. Then the angle Φ is varied (or the sample is rotated about the normal) so that **q** maps out a cone in space.

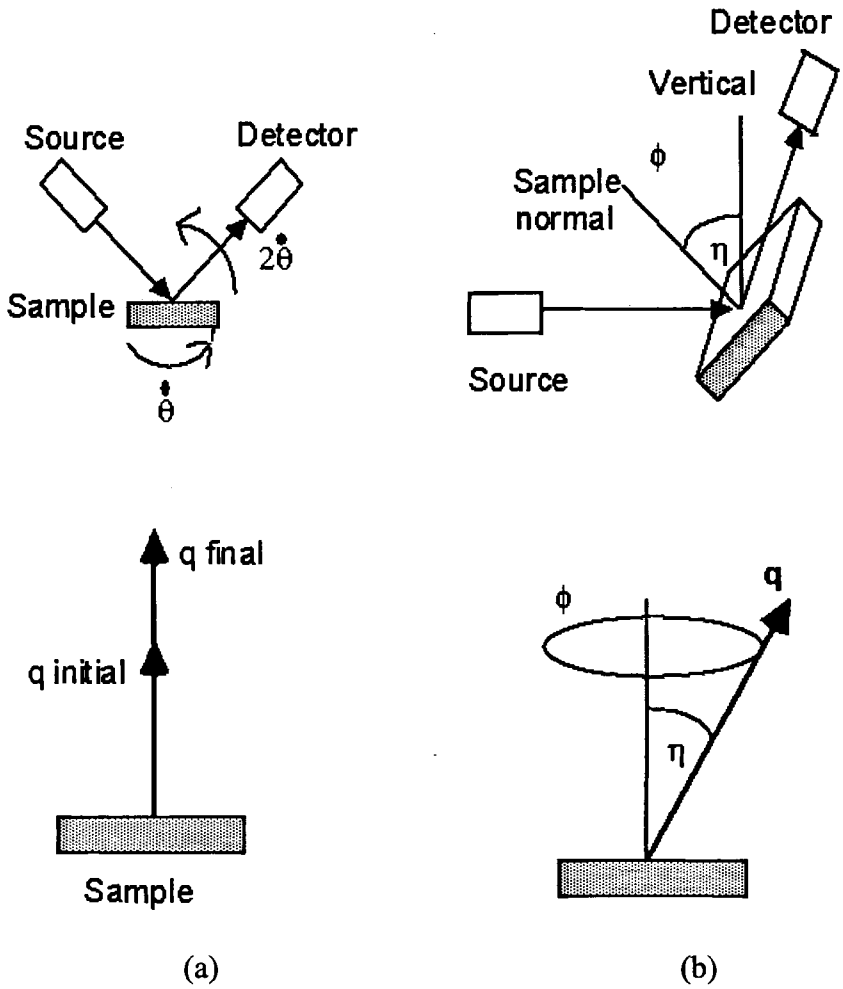

Figure 4.5: The mechanical motions of the sample and detection equipment and the motion of **q** relative to the sample for the two types of x-ray scans : a) $\theta/2\theta$ scan and b) Φ scan.

The θ/2θ scan is used to determine phase purity in the thin film sample and also distinguish between random polycrystalline orientation and textured growth shown in Figure 3.7 I and II. For the case of textured growth, a single set of diffraction peaks corresponding to a family of planes will appear, while the other diffraction peaks for the crystal will diminish or disappear entirely. The crystal direction of these planes is normal to the substrate. The Φ scan is used to determine the relative orientation of the grains *within* the plane of the substrate. If these grains are randomly oriented within the substrate plane, the diffraction intensity will be constant throughout the 360° rotation during the measurement. If the grains are preferentially oriented, diffraction peaks will appear distinctly over the 360° rotation. For complete orientation within the substrate plane, the number of diffraction peaks will correspond to the crystal symmetry of the material. For example, in a cubic crystal a Φ scan of the <110> about the <100> has four allowed peaks due to symmetry.

4.4 Results

Selective chemical vapor deposition is described in terms of the selective film growth on a particular substrate or surface.[30] It is generally used to distinguish between growth and nongrowth. Typical studies use a semiconductor or a metal as the growth surface and silica as the nongrowth surface. Examples include the selective deposition of copper and tungsten. Selective CVD can occur because of thermodynamic and kinetic limitations of deposition on the nongrowth surface. Different mechanisms for selective CVD are presented in reference 30. These include: intrinsic differences in deposition rates on

growth surfaces, the sacrificial reaction of a growth surface, the activation of a growth surface, and the selective passivation of a growth surface. In all these cases, the precursor decomposition chemistry, precursor interaction with the substrate, and substrate surface are critical in the selective CVD process.

A different type of selective CVD occurs when thin film growth occurs on two surfaces, yet one surface stabilizes a particular phase relative to the other surface, hence the phrase, phase-selective CVD. Phase-selective CVD is important in systems with multiple phases, for example, the transition metal oxides. Several transition metals form oxides with different valences resulting in distinct phases with unique properties.

Examples of controlling the particular phase (cation valence) of a transition metal oxide during CVD generally involve manipulation of the oxygen partial pressure over the growing film. These examples include the oxides of cobalt, iron, and vanadium.[31-33] For example, in a reducing atmosphere, the deposition of VO_2 is favored over V_2O_5. A unique feature of the phase selectivity between CrO_2 and Cr_2O_3 demonstrated in this work is its independence of oxygen partial pressure.

The grown CrO_2 film thickness was between 400-800Å at growth rates between 6-13Å/min. The CrO_2 films were shiny, black and highly conductive. The Cr_2O_3 films were shiny, green and highly resistive. Average roughness, as measured by atomic force microscopy, was between 30-45Å, over a $5\mu m^2$ area.

The results about stabilization of CrO_2 films on TiO_2 and Si substrates and the phase selective CVD of half-metallic CrO_2 and the antiferromagnetic, insulating, Cr_2O_3, on TiO_2 and Al_2O_3 substrates by the thermal decomposition of CrO_2Cl_2 are described.

4.4.1 The crystal structure with XRD

The decomposition of CrO_2Cl_2 on (100), (001) and (110) TiO_2 substrates in the temperature range of 330-370°C resulted in respective (100), (001) and (110) epitaxial CrO_2 thin films. At temperatures below 330°C the growth rate was negligible. The $\theta/2\theta$ x-ray diffraction scan for typical CrO_2 films grown in this temperature range is shown in Figure 4.6. In Figure 4.6(a), the peak at $2\theta = 41°$ is indexed as the (200) CrO_2 peak. Scans over the 2θ range from $10 \sim 90°$ revealed only the (200) and (400) peaks of CrO_2 indicating complete orientation with respect to the (100) TiO_2 substrate.[21] No peaks for Cr_2O_3 were observed. The electronic and magnetic properties, including spin-polarization, of these films was reported in reference 21.

The phase purity and orientation of a (110) CrO_2 film grown on a (110) TiO_2 substrate can be determined by analysis of Figure 4.6(b). Likewise, the phase purity of a (001) CrO_2 film grown on a (001) TiO_2 substrate can be determined by analysis of Figure 4.6(c). In both cases, no Cr_2O_3 peaks were observed. Also, no other peaks of CrO_2 were observed indicating complete orientation with respect to the substrate normal direction.

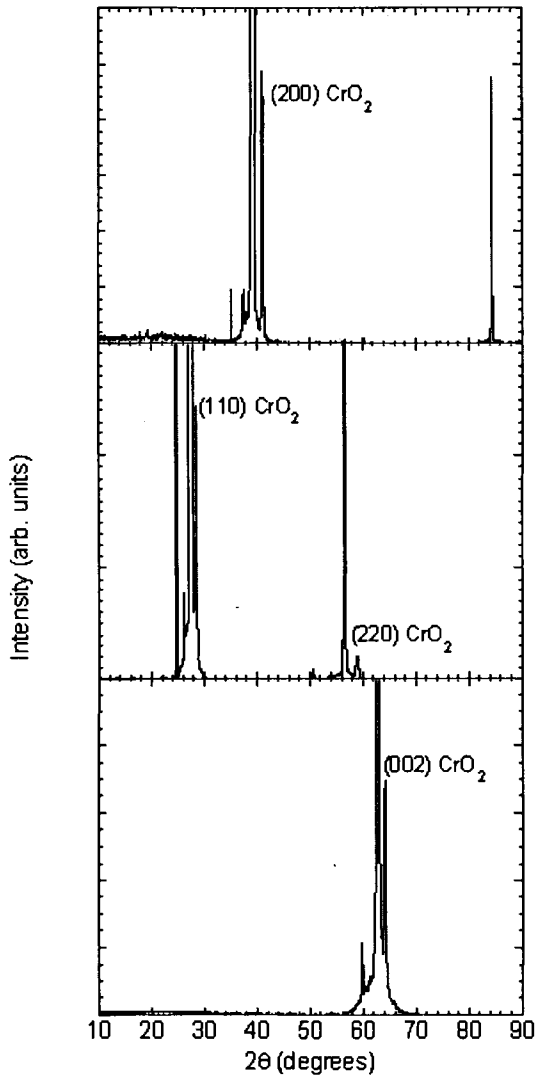

Figure 4.6: X-ray diffraction $\theta/2\theta$ scans of CrO_2 films on (a) (100) TiO_2, (b) (110) TiO_2 and (c) 001 TiO_2 substrates. The labeled peaks are CrO_2 film peaks. The substrate peaks having the corresponding indices are off-scale.

Φ-scans (where $\theta/2\theta$ is set for a particular reflection at an angle ψ to the film normal, and the film is rotated about the film normal) were performed to examine the samples for misoriented grains. For (100), (110) and (001) oriented films, Φ scans were performed about the (110), (200) and (111) planes, respectively (Figure 4.7). In all three

orientations, the measured symmetry confirmed complete grain orientation within the substrate plane. These measurements, combined with the θ /2θ scans, indicated complete epitaxy with respect to the substrate.

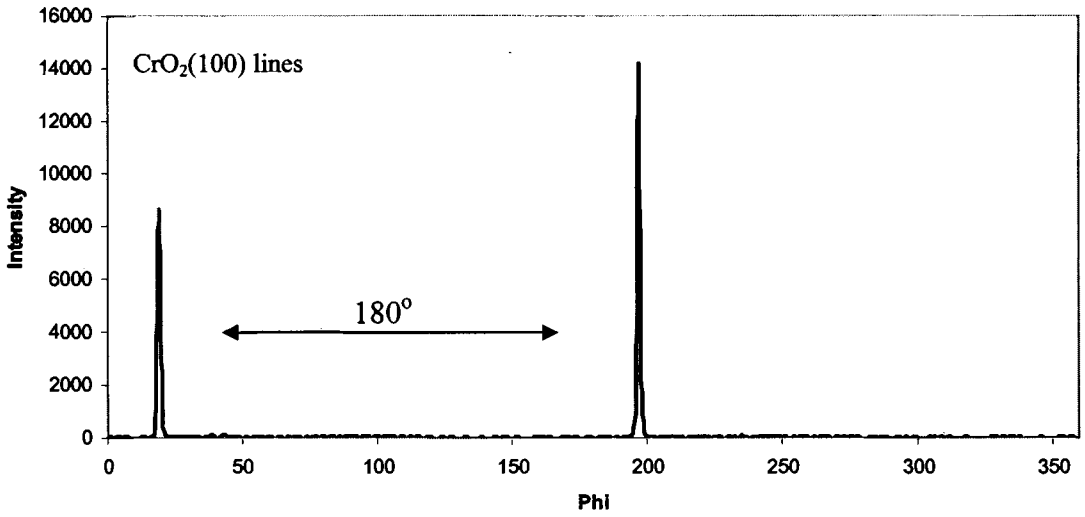

(a)

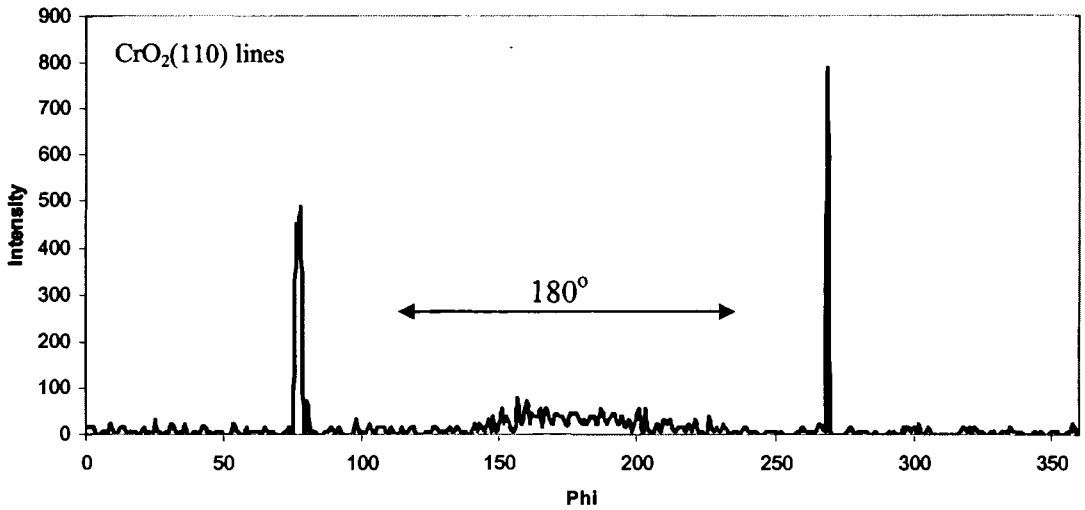

(b)

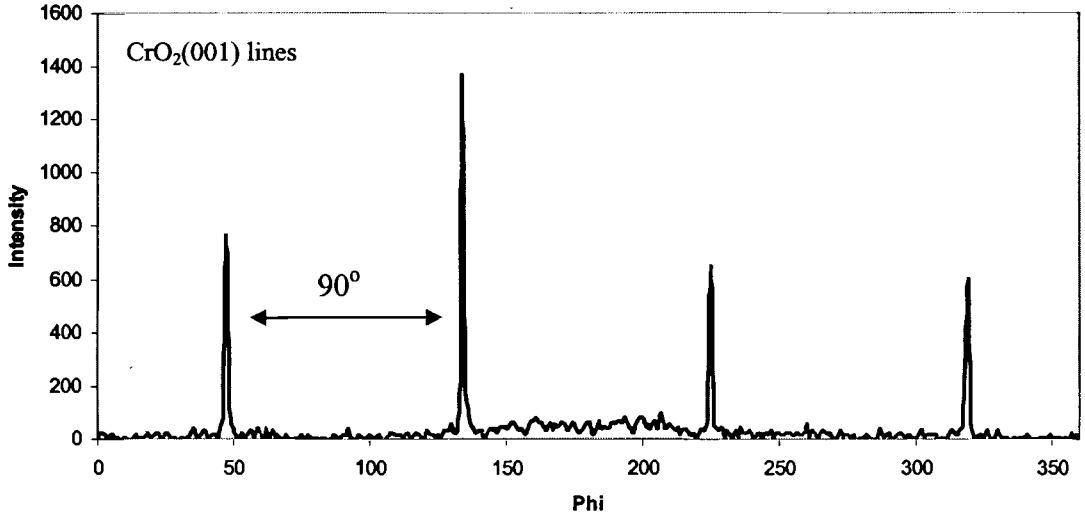

(c)

Figure 4.7: The phi scan on the (a) CrO_2 (100) line showing expected two-fold symmetry, (b) CrO_2(110) line showing expected two-fold symmetry, and (c) CrO_2(001) line showing expected four-fold symmetry

The decomposition of CrO_2Cl_2 on (0001) Al_2O_3 substrates at temperatures between 320 and 380°C resulted in (006) oriented Cr_2O_3 films. This is evidenced by the (006) feature in the x-ray diffraction scan shown in Figure 4.8(a). In contrast to the black, shiny, metallic films of CrO_2, the Cr_2O_3 films were green and insulating. As shown in Figure 4.8(a), the (200) CrO_2 peak is completely absent. In addition, the decomposition of CrO_2Cl_2 on (1012) Al_2O_3 substrates resulted in the deposition of (012) oriented Cr_2O_3 over all temperature ranges in this study.

At decomposition temperatures above 380°C, mixed CrO_2 and Cr_2O_3 films were observed on the TiO_2 substrates. At a decomposition temperature of 420°C only the Cr_2O_3 phase was identified by x-ray diffraction. The Cr_2O_3 phase was (110) oriented with respect to the (100) TiO_2 substrate.

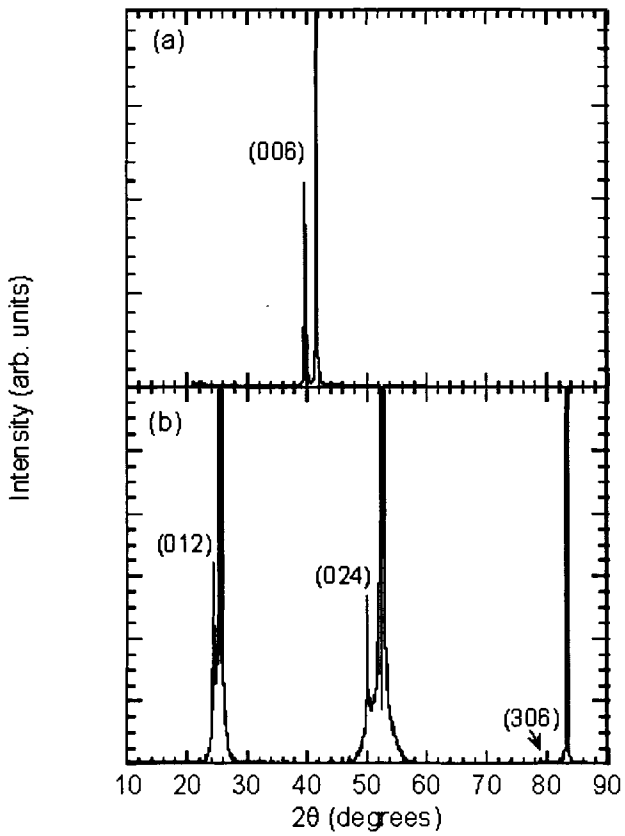

Figure 4.8: X-ray diffraction $\theta/2\theta$ scans of Cr_2O_3 films on (a) (0001) Al_2O_3 and (b) (1012) Al_2O_3 substrates. The labeled peaks are the Cr_2O_3 film peaks. The substrate peaks having the corresponding indices are off-scale.

The decomposition of CrO_2Cl_2 is quite different from the decomposition of CrO_3. Experiments performed using CrO_3 as a precursor at growth temperatures of 400°C resulted in (200) oriented CrO_2 films deposited on both (100) TiO_2 and (0001) Al_2O_3 substrates. These films are also oriented with respect to the substrate normal. These results are consistent with other reports in the literature regarding CrO_3 decomposition.[38] The results described above indicate a phase selective chemical vapor deposition reaction

that depends upon the substrate chosen. These results are unique to the CrO_2Cl_2 precursor. CVD with CrO_3 as a precursor does not result in phase selective chemical vapor deposition between Al_2O_3 and TiO_2 substrates.

It is interesting to compare the decomposition of CrO_3 and CrO_2Cl_2 under similar experimental conditions. Both precursors are strong oxidizing agents. The stabilization of CrO_2 on TiO_2 substrates is evidenced using both precursors and the dominating factor is presumed a strong templating effect of the isostructural substrate. However, the difference in reaction (of the two precursors) on the Al_2O_3 substrates remains unexplained. This suggests that the decomposition pathway of each precursor is very different, and highly influenced by the chosen substrate. We will pursue infrared spectroscopic measurements to elucidate the reaction mechanisms underlying this interesting phase selectivity.

The $\theta/2\theta$ scan of the (001) peak of the CrO_2 film and the substrate with different film thickness are shown in Figure 4.9. The lattice mismatch between the TiO_2 substrate (a=b=4.59Å, c=2.96Å) and the CrO_2 film (a=b=4.421Å, c=2.916Å) are significant, being -3.87% and -1.65% along [010] and [001] directions. When the CrO_2 film is deposited on the TiO_2 substrate, interfacial strain takes place due to lattice mismatch. As the CrO_2 film is stretched out to fit onto lattice of TiO_2 substrate, the film interplanar distance decreases. Therefore, the measured interplanar distance in the CrO_2 film is less than the one of ideal CrO_2 film. This results in the deviation of the CrO_2 peaks from ideal x-ray 2θ bulk value. As the films are thin, strains in the film due to the lattice mismatch is increased and the thinner films show the largest deviation from the bulk value. As the film grows thicker, relaxation from the strain occurred due to lattice mismatch takes

place. However, the relaxation is so slow that even films 1000Å thick show significant deviation from the bulk value.

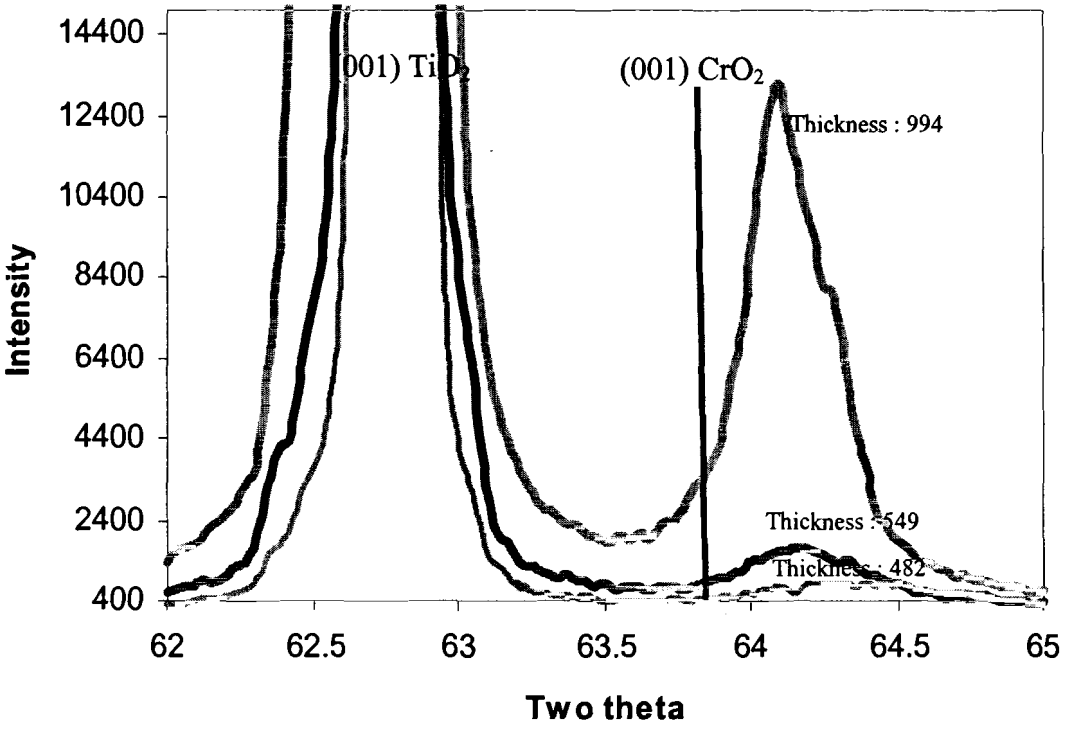

Figure 4.9: The θ/2θ scan for (001) peak of the CrO_2 films of different thickness deposited on the (001) TiO_2 substrates

4.4.2. Thin film roughness with AFM

The surface morphology of the CrO_2 thin films deposited on TiO_2 substrate was measured using atomic force microscopy (AFM) as a function of growth temperature and precursor concentration. From the AFM scans, CrO_2 film roughness was measured.

To obtain CrO_2 films with smooth surfaces, two factors were controlled: growth temperature and carrier gas flow rate.

4.4.2.1 Atomic force microscope (AFM)

The atomic force microscope (AFM), Figure 4.10, explores the surface of a sample with a sharp tip, a couple of microns long and less than 10μm in diameter. The tip is located at the end of a cantilever that is 100 to 200 mm long. Forces between the tip and the sample surface cause the cantilever to bend. A detector measures the cantilever deflection as the tip is scanned over the sample, or the sample is scanned under the tip. The measured cantilever deflections allow a computer to generate a map of surface topography. AFM can be used to study insulators and semiconductors as well as electrical conductors.[40]

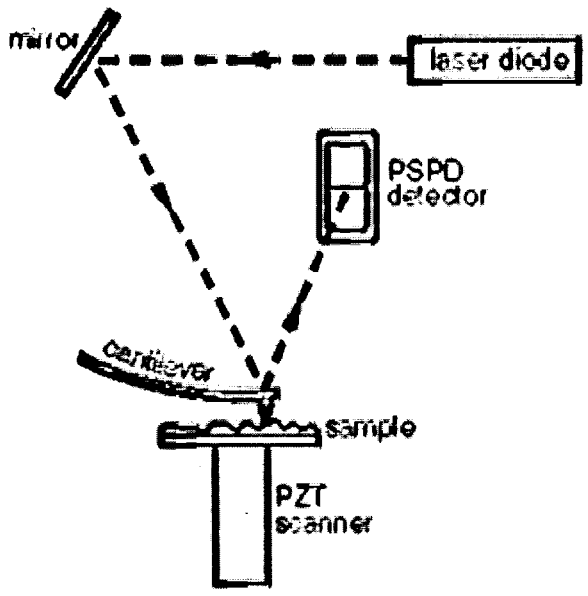

Figure 4.10: AFM mechanism

4.4.2.2 Analysis CrO_2 thin film with growth temperature

In Figure 4.11, the rms (root mean square) roughness for CrO_2 films deposited on the TiO_2 substrate is shown for a variety of growth temperatures.

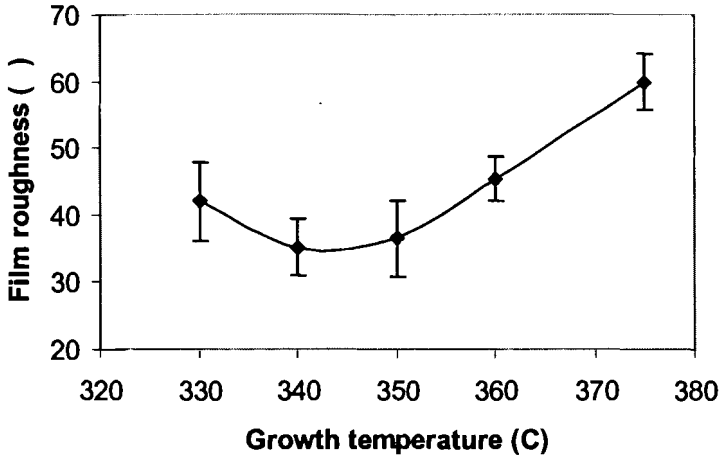

Figure 4-11: The rms roughness for CrO_2 thin film deposited on the TiO_2 substrate at various growth temperature. Error bars represent ±one standard deviation.

The rms roughness values range from 33 to 58 with an average standard deviation of 5.8 . The film roughness first decreases with increasing growth temperature and then starts to increase above 350°C. Below 340 °C, the grain coalescence does not happen because the vertical grain growth rate is faster than the lateral growth rate. Film roughness results from this reason. Above 360 °C, the surface roughness starts to increase again. As the growth temperature goes up, the grain size also increases. In Figure 4.12, the comparison of grain sizes at different growth temperature is shown in AFM picture. The AFM scan range was 5μm x 5μm. As the grain size increase, the depths of grain valleys also increases, which leads to a rough surface. From the simple equation, rms

roughness can be expressed by the following relationship.[41]

$$\sigma = r_0^2/2[H]$$

where σ is the rms roughness, r_0 is the average grain radius and [H] is the average film thickness. From this equation, roughness is proportional to the grain radius. Therefore, as the grain size is small, the film roughness also decreases. Consequently, there are two factors affecting film roughness. First, the lattice mismatch between CrO_2 and TiO_2 produces strain within the film resulting in a three dimensional grain growth mechanism, particularly at lower temperature. Three dimensional growth mechanisms in thin film lead to columnar structures with poor grain coalescence. Second, at higher temperature, larger grains form resulting in deeper grooves at the grain boundary, and hence, rough surfaces.

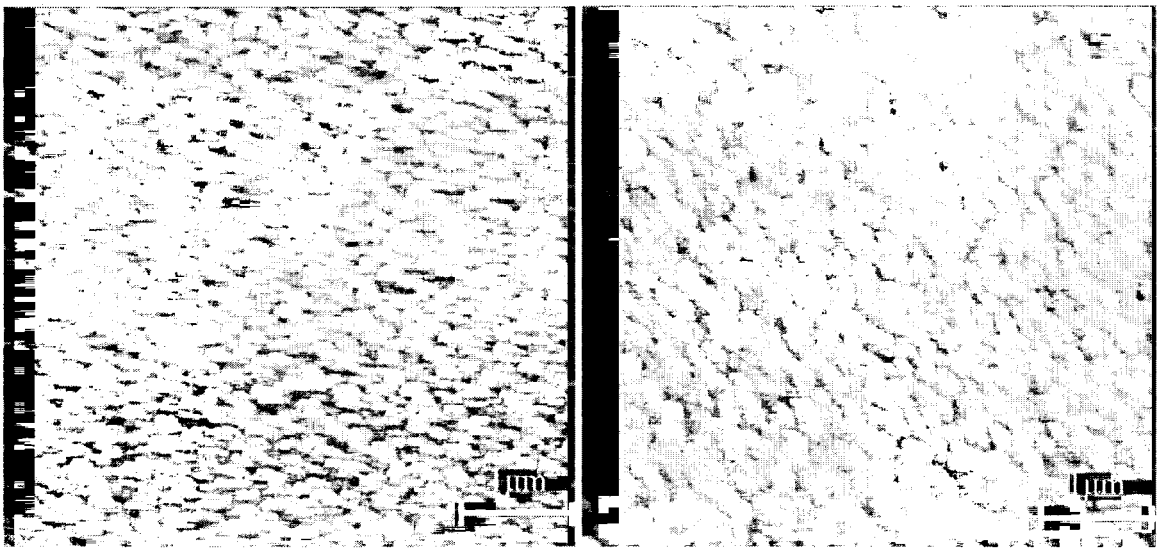

320 °C, 40sccm
Roughness 42Å

370 °C, 40sccm
Roughness 60Å

Figure 4.12: The surface morphology of CrO_2 film deposited on the TiO_2 substrate at two different growth temperatures

4.4.2.3. Analysis CrO_2 film with carrier gas flow rate

The nucleation density is a function of carrier gas flow rate and substrate temperature. Therefore, film roughness is also affected by the carrier gas flow rate, which is used to control precursor concentration in the reactor. In Figure 4.13, the relationship of film roughness and carrier gas flow rate is shown.

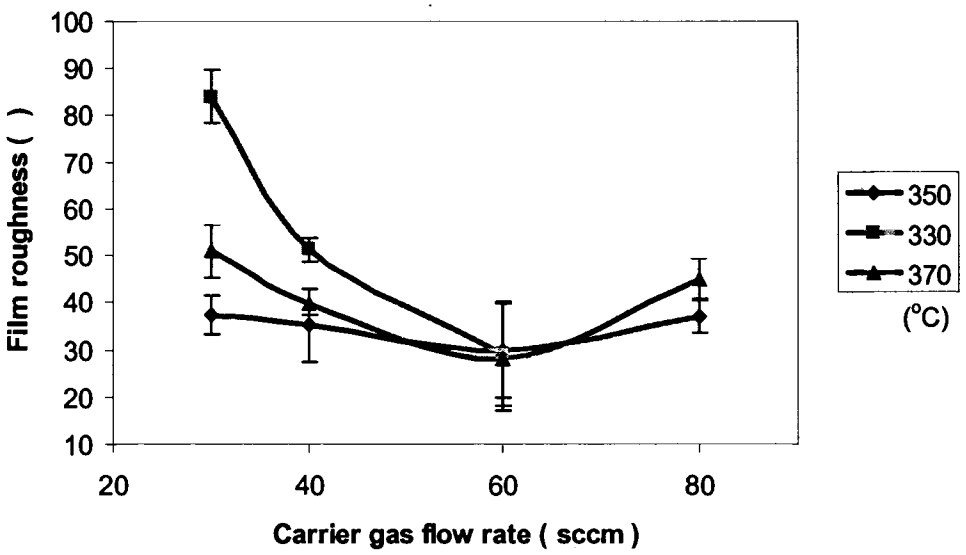

Figure 4.13: The rms roughness with increasing carrier gas flow rate.
Error bars represent ±one standard deviation.

To observe the effect of grain growth and coalescence, CrO_2 films were grown at different carrier gas flow rates. The roughness standard deviation is 10.43 . At low carrier gas flow rates, below 50 sccm, a large number of discontinuous grains are first formed, but complete coalescence has not yet occurred. After reaction for several minutes, individual grains slowly coalesce. After the grains merge, the grain size is considerably larger, forming deep grain boundary valleys. The resulting film surfaces

are very rough as shown in the AFM images in Figure 4.14.

When the carrier gas input is increased to 50 ~ 60 sccm, the precursor concentration and flux in the reactor is increased and the nucleation density is increased. Therefore, grain coalescence is rapid. After coalescence, grain growth is severely limited because there are no spaces for individual grains to grow. As a result, these film surfaces are smooth. Above a flow rate of about 60sccm, the film roughness starts to increase. High carrier gas flow rates reduce the precursor residence time, resulting in incomplete decomposition of the precursor. As the flow rate was continually increased, the film surfaces became rough to the naked eye and had poor quality.

In Figure 4.14, the AFM images of CrO_2 films grain with different carrier gas flow rates are shown. At 60sccm, the grain size is smallest, became of the small grain boundary valley depth and smooth surface. At 20sccm, many voids are observed, which leads to larger grains. As explained previously, films with larger grains generally have rough surfaces.

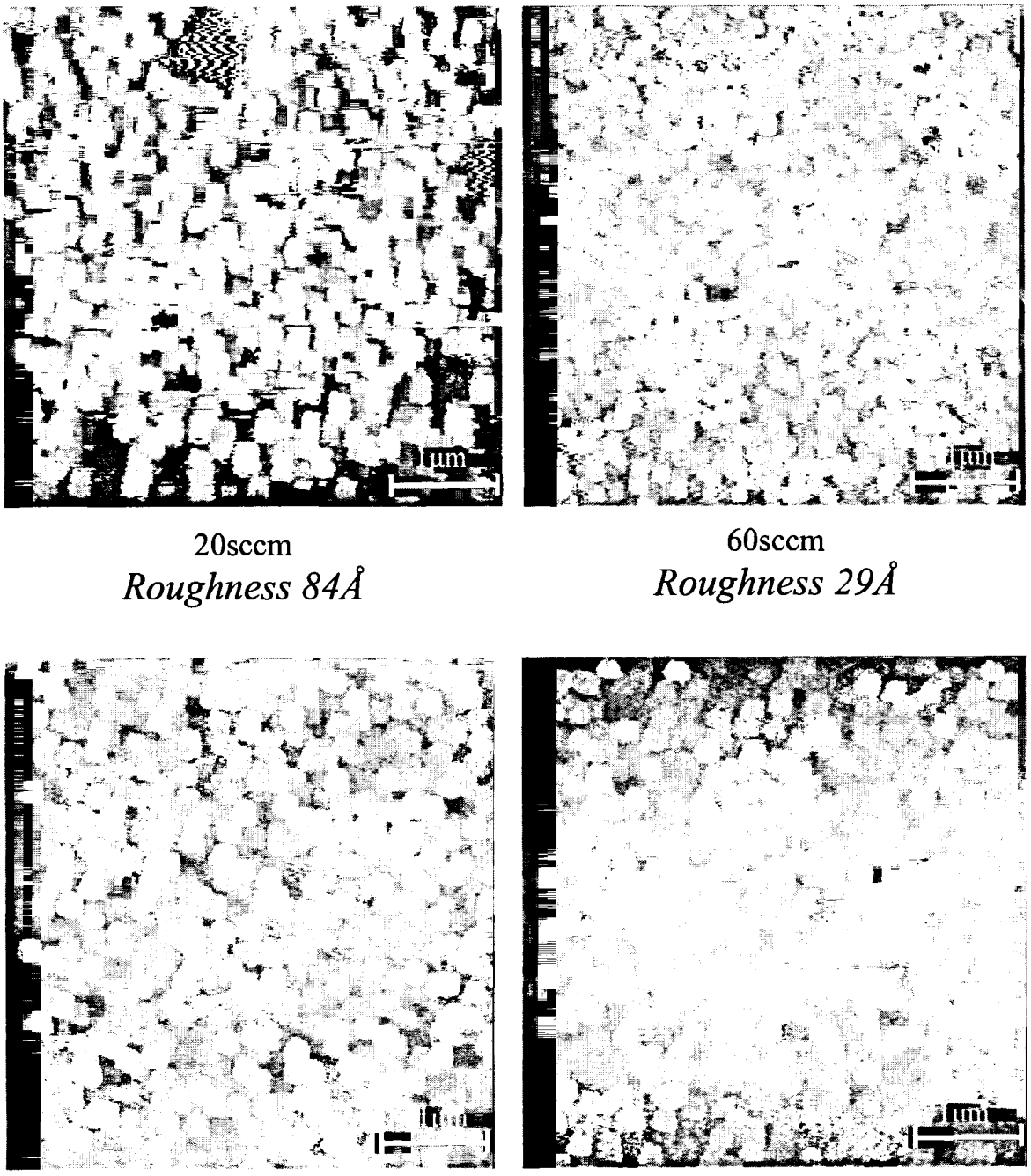

Figure 4.14: The comparison of film roughness as a function of carrier gas flow rate

4.4.3 $CrO_2/TiO_2/BaF_2/Si$ multilayer fabrication with chemical vapor deposition

To be compatible with existing semiconductor process, techniques would like to fabricate GMR device on Si substrates. Unfortunately, however, CrO_2 thin films cannot be deposited directly on Si substrates for a couple of reasons. First, the crystal structures between Si and CrO_2 are completely different: Si substrate has a cubic structure and CrO_2 has a tetragonal crystal lattice. Second, Si substrates react with some oxide compounds, forming silicides and mixed oxides. To fabricate a CrO_2 film on a Si substrate, intermediate layers are required. As a solution, crystalline rutile TiO_2 films have been deposited on BaF_2/Si films at LASST, and these TiO_2 layers were found suitable substrates for CrO_2 deposition.

4.4.3.1 Experimental procedures

The experimental procedure for depositing CrO_2 thin films on the $TiO_2/BaF_2/Si$ substrate was similar to that described in section 4.2.

4.4.3.2 Results

4.4.3.2.1 The crystal structure with XRD

Figure 4.15 shows the XRD pattern of $CrO_2/TiO_2/BaF_2/Si$ thin film at 350°C by CVD.

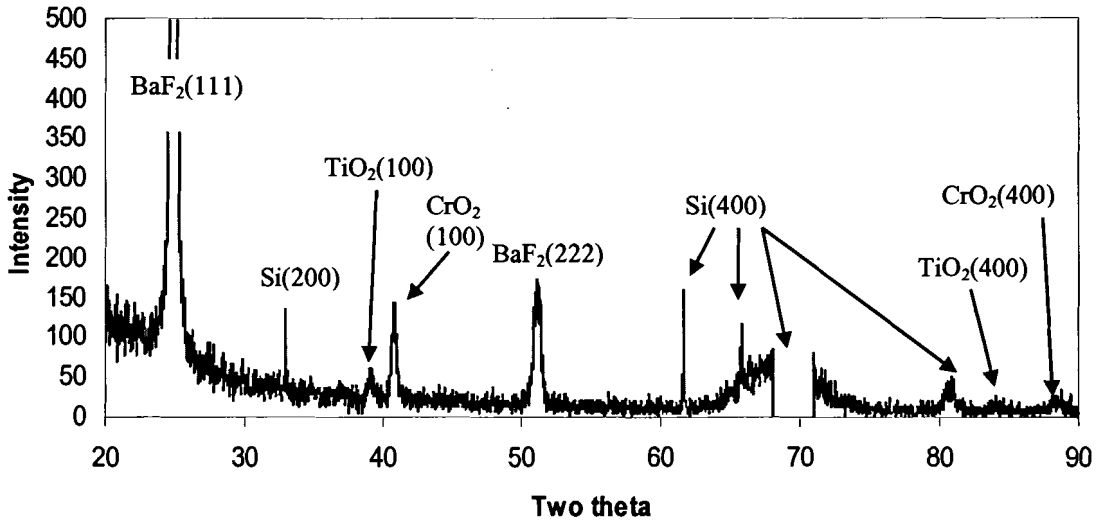

Figure 4.15: The XRD pattern of $CrO_2/TiO_2/BaF_2/Si$ thin film

CrO_2 (100) thin film were successfully deposited on the Si substrate by CVD using intermediate layers such as TiO_2 and BaF_2. There are no peaks for impurities. As seen in Figure 4.15, the BaF_2 was <111> oriented normal to the Si (100) substrate. The TiO_2 film grows in the <100> direction normal to the Si (100) substrate. The CrO_2 film matched the TiO_2 orientaion normal to the substrate plane. Figure 4.16 shows the phi scan for in-plane symmetry of $CrO_2/TiO_2/BaF_2/Si$ thin film.

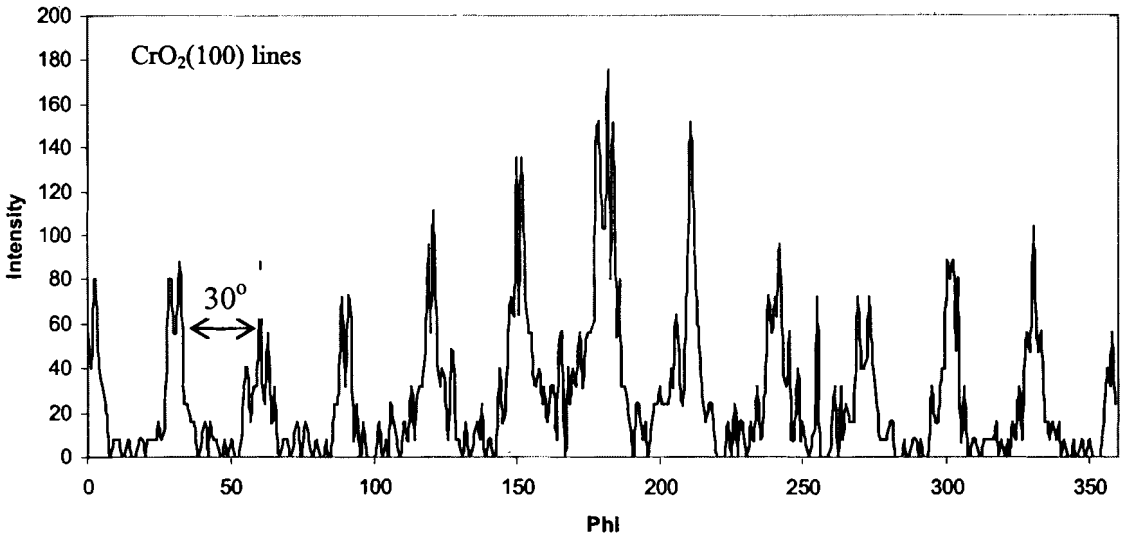

Figure 4.16: The phi scan for $CrO_2/TiO_2/BaF_2/Si$ thin film

The TiO_2 (100) film had 12-fold symmetry in the substrate plane. The CrO_2 (100) film grows in complete orientation to the TiO_2 film and also had 12-fold symmetry. This film is less crystalline than the films grown on single crystal substrates and is expected to have large angle grain boundaries.

4.4.3.2.2 The spin polarization

To detect spin polarization of a CrO_2 thin film grown on a Si substrate, a film was sent to the Naval Research Laboratory (NRL). They used the technique of point-contact Andreev reflection to determine the spin polarization of the CrO_2 thin film. From this experiment, the CrO_2 film deposited on Si substrate using intermediate layers had been observed to achieve spin polarization of ~70%. Based on the theory, CrO_2 is expected to

have 100% spin polarization. This discrepancy can be explained in part, by the interior crystalline quality of the CrO_2 film.

4.5 Conclusion

Using CrO_2Cl_2 as a precursor, CrO_2 thin films have been deposited epitaxially on TiO_2 substrates by chemical vapor deposition. The CrO_2 thin films also could be stabilized on Si substrates using intermediate layers. The CrO_2 films show a black, shiny appearance. The grown films are smooth, highly conducting and spin-polarized. We have observed interesting phase selectivity of CrO_2Cl_2 decomposition and attempted to elucidate the reaction mechanism underlying this interesting phase selectivity using ex-situ FT-IR. However, ex-situ FT-IR was not suitable for investigation of the mechanism responsible for this. Future studies using in-situ techniques would be useful. CrO_2 films are promising for GMR devices. At next section, the sandwich structures of CrO_2/RuO_2 can be fabricated. These sandwiches will be able to amplify the GMR effect.

CHAPTER 5

RuO_2 THIN FILM FABRICATION WITH METALORGANIC CHEMICAL VAPOR DEPOSITION

5.1 Introduction

RuO_2 crystallizes in the rutile structure (tetragonal with a = b = 4.499 , c = 3.107) and is metallic with a room temperature resistivity of 40 μΩ-cm. RuO_2 is non-magnetic, thermally stable and chemically stable. RuO_2 can be an exciting candidate as the non-magnetic layers in a GMR device based on the completely spin-polarized CrO_2. RuO_2 is isostructural with CrO_2 having the potential to create epitaxial multilayer structures. RuO_2 also will not form solid solutions with CrO_2 leading to the potential for clean interfaces between these two materials, which is necessary for optimal GMR behavior. In addition to the above applications, RuO_2 films have primary applications as conductive and diffusion barrier layers in ultra-large scale integrated (ULSI) circuits; particularly circuits involving high dielectric oxide materials such as ferroelectrics (e.g., $BaTiO_3$).[42-49]

Thin films of RuO_2 have been prepared by a variety of techniques including sputtering and chemical vapor deposition (CVD).[42-49] Typical substrates chosen for these experiments were Si, SiO2, and MgO. To our knowledge, the use of TiO_2 rutile single crystal substrates to stabilize epitaxial RuO_2 has not been attempted. It is the purpose of this work to investigate the deposition of RuO_2 on single crystal TiO_2 and CrO_2/TiO_2 substrates by CVD. Particular attention is given to overlapping thermodynamic processing space between CrO_2 and RuO_2 thin films. This is fundamentally critical for

establishing a multilayer deposition process that is highly controlled, minimizes intermixing at the interface, and maintains high spin-polarization and conductivity in the individual layers of the structure.

5.2 Experimental technique for RuO_2 thin film fabrication

RuO_2 films were deposited in a horizontal, hot-wall CVD reactor shown in Figure 5.1. The precursor, $[(C_{11}H_{19}O_2)_2(C_8H_{12})Ru$, Ru-TMHD] followed by the formula (Ru-TMHD), was sublimed in a bubbler heated to 100°C. Argon, used as a carrier gas, transported the Ru-TMHD into the heated reactor where it decomposed on the TiO_2 or CrO_2/TiO_2 substrate. Oxygen was introduced to assist in the thermal decomposition of Ru-TMHD. Typical flow rates of argon and oxygen were 140 to 200sccm and 0 to 350sccm, respectively.

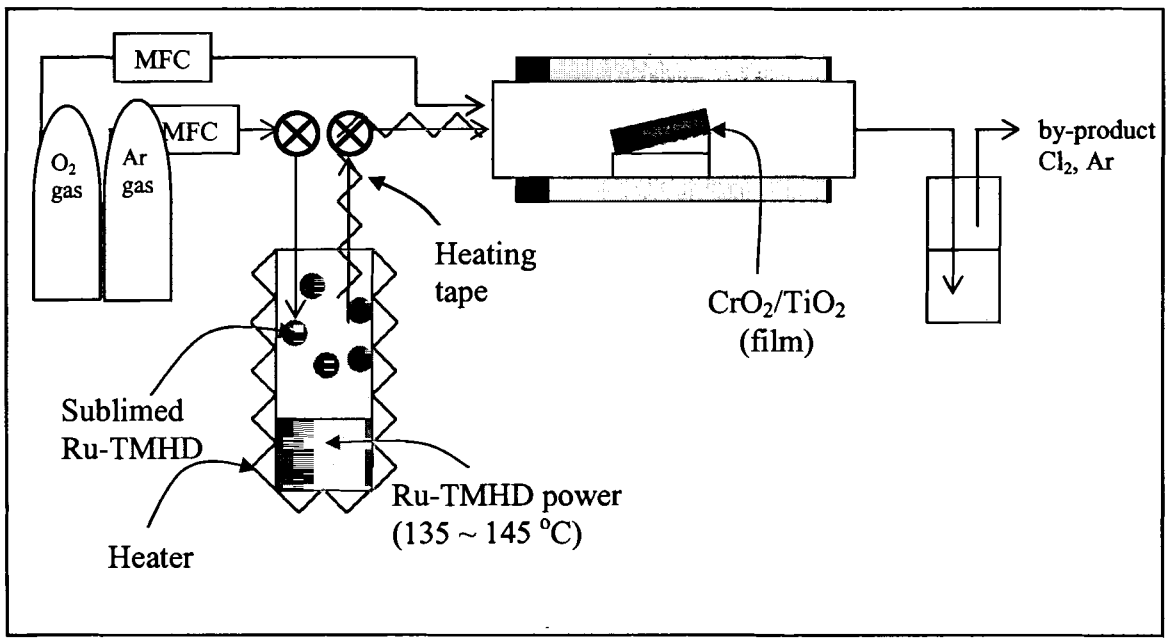

Figure 5.1: The apparatus for RuO_2 thin film on the CrO_2/TiO_2 film

To avoid condensation of the precursor, all surfaces of the gas delivery system were wrapped in heating tape and maintained at a temperature higher than the bubbler temperature. TiO_2 single crystal substrates in (001) orientation were cleaned in acetone, methanol, 2-propanol and DI water, followed by a cleaning in a 20% HF solution. Substrate temperatures were varied between 250 and 450°C. Deposition conditions are listed in Table 5.1.

Table 5.1: Deposition condition of RuO_2 thin films

Source material	Source temperature (°C)	Carrier gas flow rate (sccm)	Reaction gas flow rate (sccm)	Substrate temperature (°C)
Ru-TMHD	135 to 145	140 to 200	0 to 350	250 to 450

The thickness of the RuO_2 films was measured by profilometry (Dektak). Since no wet etchant is known for RuO_2, films grown on (001) CrO_2/TiO_2 substrates were used. The RuO_2 film was patterned with a photoresist and the resulting CrO_2 underlayer was etched using a chromium etchant. This technique is referred to as lift-off and is shown in Figure 5.2. X-ray diffraction was used to determine phase purity and orientation of the film normal to the plane via standard $\theta/2\theta$ measurements. ϕ-scans were used to determine the symmetry of the RuO_2 film in the substrate plane. Surface morphology and roughness were measured with an atomic force microscope (AFM).

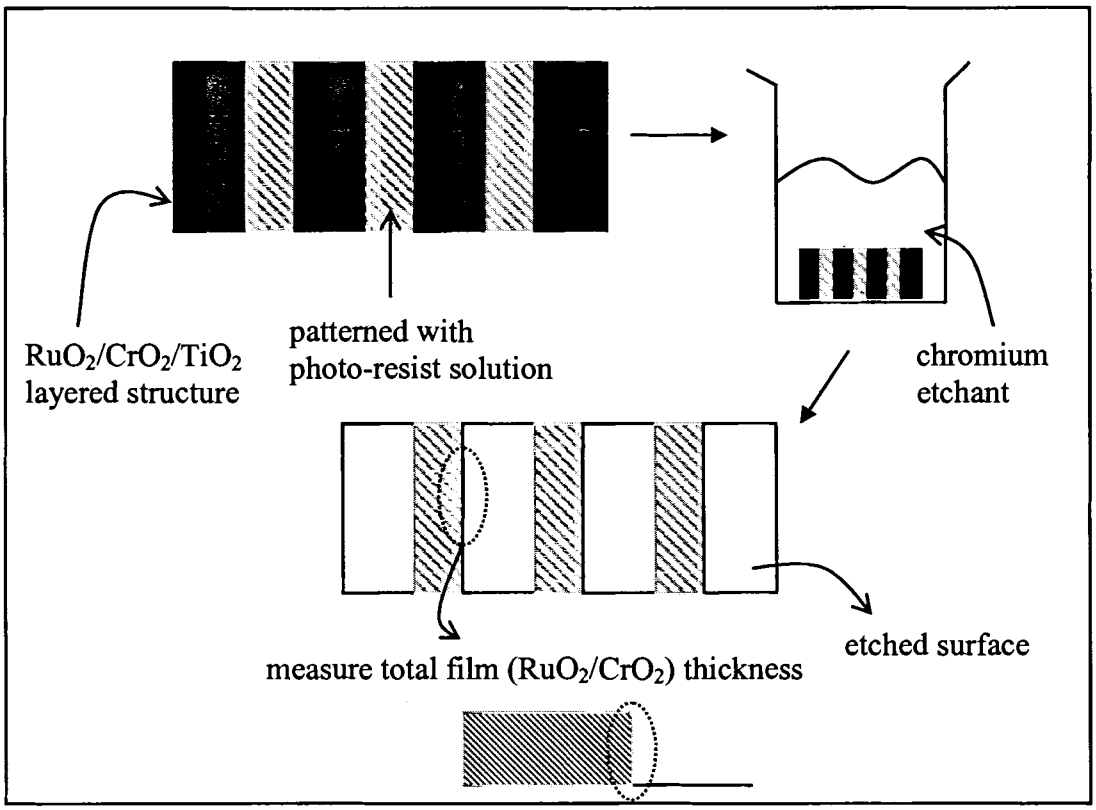

Figure 5.2: The procedure for measuring RuO_2 thin film on the CrO_2/TiO_2

5.3 Results

RuO_2 thin films were deposited on (001) TiO_2 and (001) CrO_2/TiO_2 substrates in the temperature range of 250-450°C. The growth rates were 2-4Åmin^{-1} resulting in films with thicknesses between 100 and 500Å. The films were crack-free, reflective and well-adhered to the substrate. The films had a shiny, dark blue appearance. RuO_2 films were deposited with and without oxygen addition. The deposition of RuO_2 films without oxygen addition is unique to this study and may be facilitated, in part, by the use of TiO_2 substrates.

Figure 5.3 shows an x-ray diffraction pattern (θ/2θ) for a RuO_2 film deposited on a (100) CrO_2/TiO_2 substrate at 280°C with an oxygen flow rate of 350sccm. The XRD pattern shows the RuO_2 single phase appearing with (100) orientation, matching the orientation of the substrate. No impurity peaks were observed.

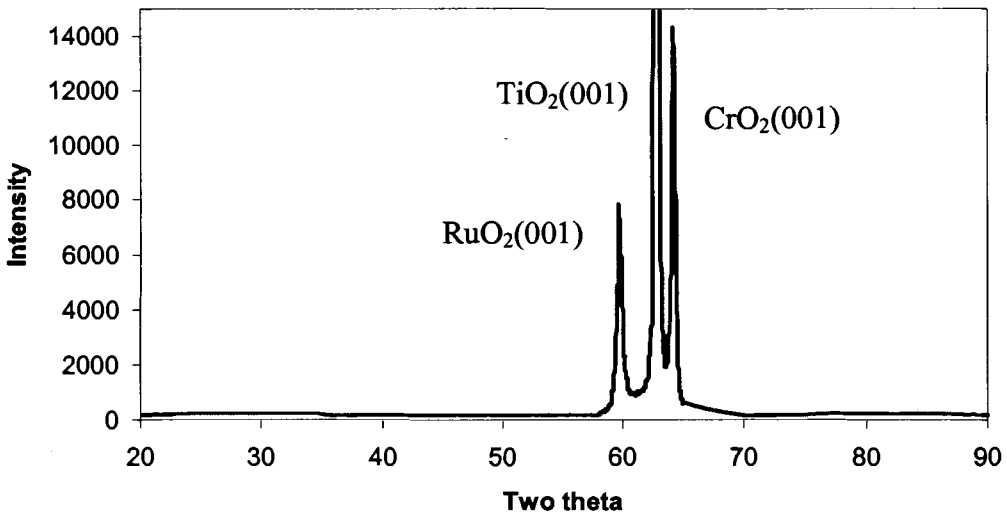

Figure 5.3: The XRD pattern of $RuO_2(001)$ film on the $CrO_2(001)/TiO_2(001)$ substrate at temperature 280°C

Figure 5.4 shows the XRD (θ/2θ) patterns of RuO_2 films deposited at temperatures from 270 and 420°C, all with oxygen added as a reaction gas. The (001) RuO_2 peak is observed with deposition temperatures as low as 270°C.

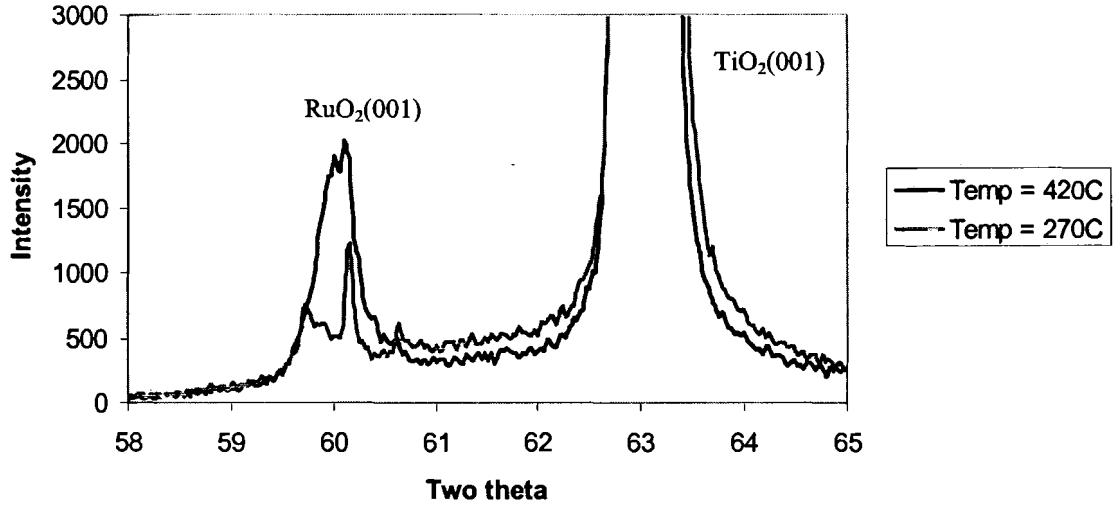

Figure 5.4: The XRD patterns for RuO_2 film on the $TiO_2(001)$ substrate at deposition temperature of 270 °C and 420 °C

Figure 5.5 shows the XRD ($\theta/2\theta$) patterns of (001) RuO_2 films deposited at 320°C at various oxygen flow rates. The (001) peak of the film deposited with 25sccm of oxygen added was considerably broader indicating a less crystalline film. These results are consistent with the surface morphology and roughness measurements which revealed a significant surface roughening effect as oxygen flow was reduced. Clearly, the oxygen plays a critical role in the decomposition pathway of the Ru-TMHD precursor.

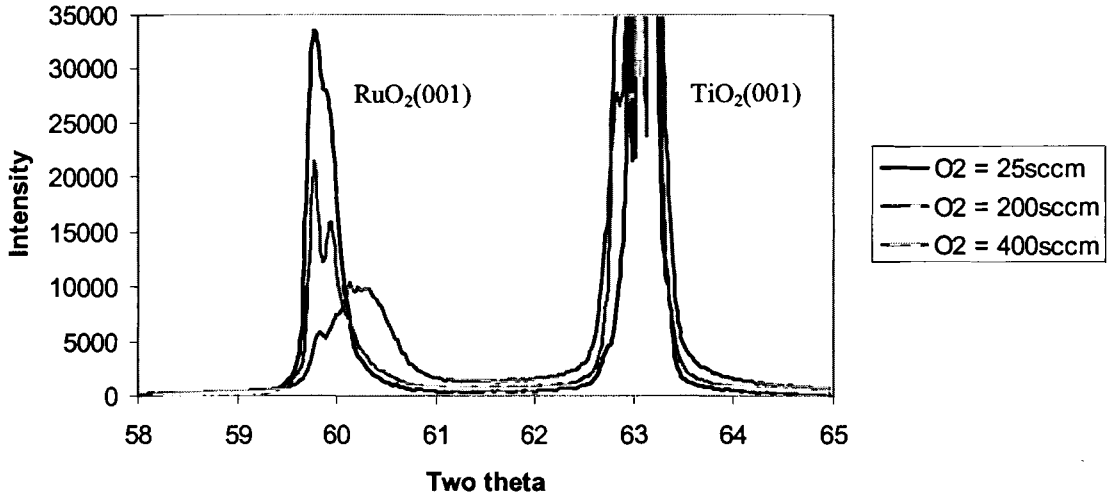

Figure 5.5: The XRD patterns of $RuO_2(001)$ film on $TiO_2(001)$ substrates at various oxygen flow rates 25 ~ 400sccm

Figure 5.6 shows a phi-scan performed about the (111) plane. In the tetragonal structure where a=b, the expected symmetry of the (111) plane about the c-axis is expected to be four-fold. The phi scan for this film reveals four sharp intensities of the (111) plane, 90° apart, indicating a four-fold symmetry. This confirms the complete registry of the (001) RuO_2 film with the (001) TiO_2 substrate.

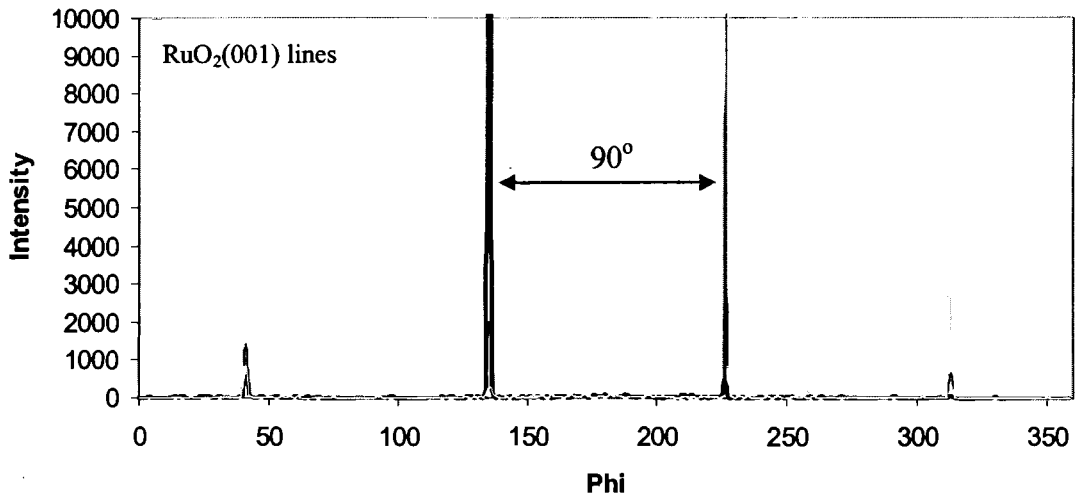

Figure 5.6: The phi scan on the RuO_2 (001) line showing expected four-fold symmetry around the (111) direction

Figure 5.7 shows the surface morphologies of (001) RuO_2 films deposited with varying amounts of oxygen added. The film surface became smoother as the amount of oxygen was increased. Apparently the addition of oxygen increased the nucleation rate leading to smaller grains which coalesced more quickly, leading to a smoother surface. One possible explanation for this is that adsorbed oxygen on the growth surface increases the kinetics of decomposition of the Ru-TMHD precursor. Unfortunately, this could not be examined by measuring growth rates because the growth rates of films were all very low under all processing conditions examined in this thesis.

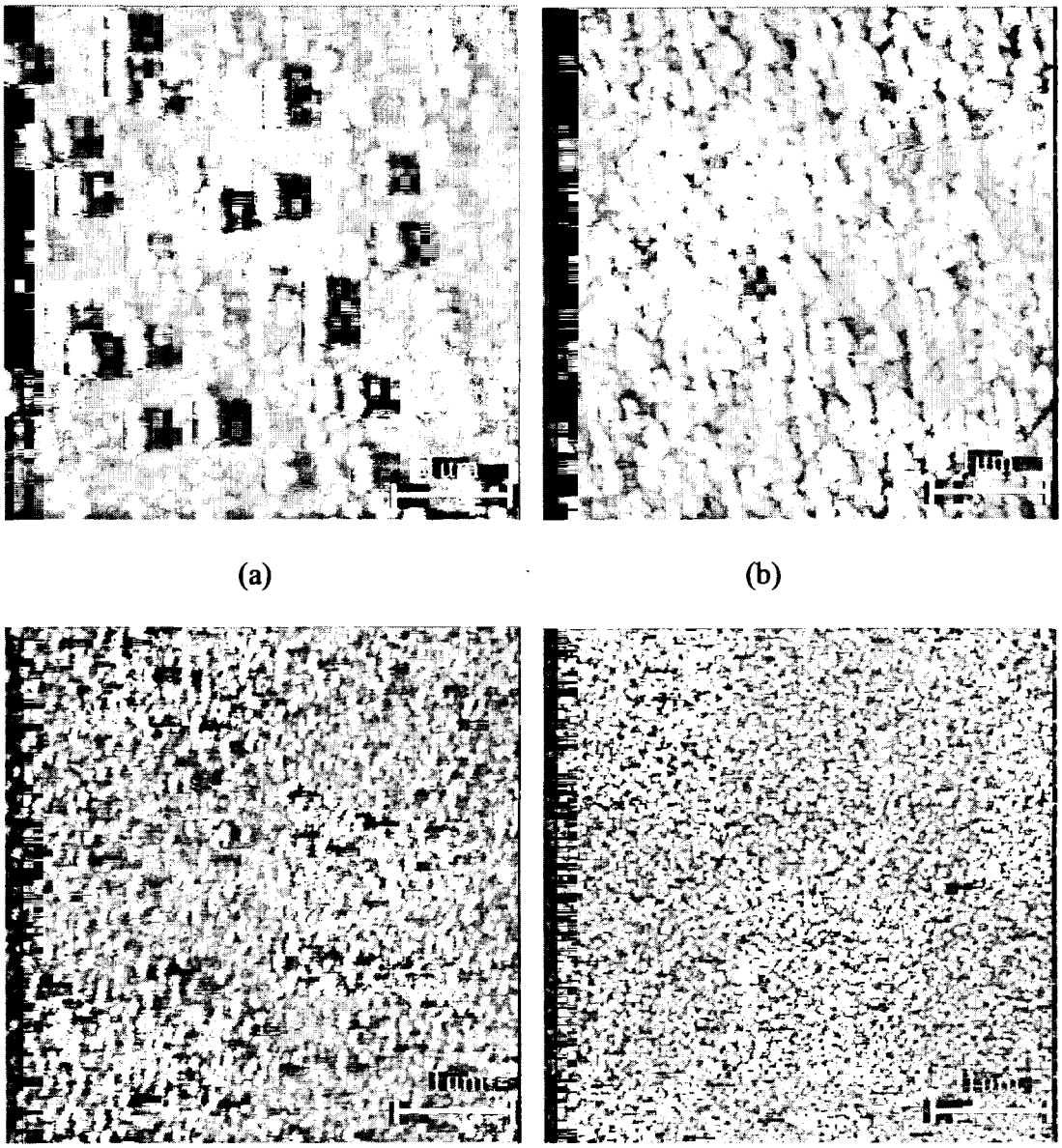

Figure 5.7: The surface morphology of RuO_2 film at various oxygen rate (a) 0sccm, (b) 25sccm, (c) 200sccm and (d) 400sccm at decomposition temperature of 320°C

5.4 Conclusion

(001) RuO_2 films were deposited on (001) TiO_2 and (001) CrO_2/TiO_2 substrates via chemical vapor deposition of Ru-TMHD. The films grew in complete registry with the substrates and no impurities were detected. Epitaxial films were deposited from 270-500°C with or without oxygen added as a reaction gas. The addition of oxygen, however, resulted in smoother films. Oxygen was suspected to increase the nucleation rate by increasing the kinetics of Ru-TMHD decomposition. Another important aspect of this work is that the thermodynamic processing window examined for RuO_2 deposition overlapped the window for CrO_2 deposition, making possible the in-situ deposition of multi-layers of these materials for GMR structures based on completely spin-polarized materials. As observed in the deposition of RuO_2 on the CrO_2 thin film, the CrO_2 film remained structurally intact and there was no evidence of intermixing as determined by x-ray diffraction.

CHAPTER 6

CONCLUSION

6.1 Summary

Despite many difficulties, the stabilization of rutile oxide films on TiO_2 substrates were successfully performed by CVD. The x-ray diffraction pattern showed epitaxial film growth on various substrates. AFM images indicated smooth film surfaces. All films appeared crack-free and well adhered to the substrate. In this thesis, CrO_2 and RuO_2 thin films, crystallizing in rutile structure, were deposited by CVD.

First, CrO_2 thin films were deposited on TiO_2 substrates at the temperature range of 330 ~ 370°C using CrO_2Cl_2 as a precursor. There have been many efforts to fabricate CrO_2 thin film due to its unique magnetic properties, especially complete spin-polarization. The decomposition of CrO_2Cl_2 showed the phase selective chemical vapor deposition between TiO_2 and Al_2O_3 substrates.

When using CrO_2Cl_2 as a precursor, CrO_2 films were deposited on TiO_2 substrates and Cr_2O_3 films were fabricated on Al_2O_3 substrate at the temperature range of 330 ~ 370°C. This suggests that the phase selective chemical vapor deposition depends on the substrate selection. However, experiments performed using CrO_3 as a precursor showed the different results;CrO_2 films were deposited on both TiO_2 and Al_2O_3 substrates. In this case, the decomposition of CrO_3 as a precursor does not result in phase selective chemical vapor deposition between TiO_2 and Al_2O_3 substrates.

Therefore, the decomposition pathway of each precursor is very different and is influenced by the substrate selection. Also, the lattice mismatch between the TiO_2 substrate and the CrO_2 film increased film strain, and showed the largest deviation from the bulk value for the thinnest films.

The surface morphology of CrO_2 film on TiO_2 substrate were observed with AFM as a function of growth temperature and precursor concentration. As the growth temperature was increased, the depth of grain valleys was also increased resulting in a rough surface. At a growth temperature of 340°C, the smoothest film was obtained. Since the nucleation density is a function of the carrier gas flow rate and the substrate temperature, film roughness is also influenced by carrier gas flow rate. At 60sccm of carrier gas flow rate, the film had the smoothest surface. At low carrier gas flow rate, many voids were observed, which leads to larger grains. High carrier gas flow rates reduced the precursor residence time resulting in incomplete decomposition of precursor.

CrO_2 films were also deposited on Si substrate using TiO_2 and BaF_2 as intermediate layers ($CrO_2/TiO_2/BaF_2/Si$). However, these films were less crystalline than those deposited on single crystal TiO_2 and they contained large angle grain boundaries. These CrO_2 films deposited on Si substrates using intermediate layers have been observed to achieve spin polarization of ~70% rather than 100% spin polarization as predicted by theory. This inconsistency results from, in part, the presence of the large angle grain boundaries in the CrO_2 films.

RuO_2 thin films that could be used as the non-magnetic metal layer in GMR device based on CrO_2 were epitaxially deposited on TiO_2 substrate using Ru-TMHD precursor in the temperature range of 250-450°C with or without oxygen addition. The oxygen played

an important role in the decomposition of the Ru-TMHD precursor and affected to the film surface morphology. Since the oxygen addition increased the nucleation rate leading to smaller grains, films had smoother surface with increased oxygen. The processing procedure observed for RuO_2 deposition overlapped the procedure for CrO_2 deposition, making possible the in-situ deposition of multi-layers of these materials for GMR structures based on completely spin-polarized materials.

6.2 Future work

Through this research, two kinds of thin films, CrO_2 and RuO_2, were deposited on the TiO_2 and Si substrates by CVD and many interesting aspects were observed. The multi-layers were also deposited as two repeated sandwiches ($CrO_2/RuO_2/CrO_2/RuO_2$). In order for these deposited films to be fabricated in GMR device, various properties will be measured. Film resistance change vs. temperature will be also investigated about this structure using four-point probe.

Since most metallic oxides crystallizing in the rutile structure have very interesting properties and a variety of industrial applications, it is also worthy of fabricating other rutile oxide materials on rutile structure substrates or Si wafers directly.

The decomposition pathway of each precursor, interaction mechanism and surface chemistry between substrates and films have not yet discovered. It would be interesting to investigate the reaction mechanism. One of the possible methods for investigating this is in-situ infrared spectroscopy.

BIBLIOGRAPHY

1. J. Belleson, E. Grochowski, "The era of giant magnetoresistive heads", 1998 http://www.storage.ibm.com/hdd/technolo/gmr/gmr.htm

2. J.H. Brunning, J.Vac.Sci. Technol. 56, 1925 (1979)

3. M.H. Kryder, W. Messener, and L.R. Carley, J. Appl. Phys. 79, 4485 (1996)

4. G.A. Prinz, Journal of Magnetism and Magnetic Materials. 200, 57 – 68 (1999)

5. B. Schechter, M. Ross, "Leading the way in Storage". http://domino.research.ibm.com/comm/wwwr_thinkresearch.nsf/pages/storage297.html

6. S. S. P. Parkin, Annu. Rev. Mater. Sci. 25, 357 - 388 (1995)

7. B. Jones, "Theory of exchange coupling in magnetic multilayers" http://researchweb.watson.ibm.com/journal/rd/421/jones.html

8. W. Zou, "Synthesis of Giant Magnetoresistive Multilayers", The materials and science Engineering department, University of Virginia (2001)

9. S.S.P. Parkin, R. Bhadra, and K.P. Roche, Physical Review Letters. 66, 2152 (1991)

10. S.S.P. Parkin, N. More, and K.P. Roche, Physical Review Letters. 64, 2304 (1990)

11. G. A. Prinz, Science. 282, 1660 (1998)

12. G. A. Prinz, Physics Today, 58 (1995)

13. P. M. Levy, Journal of Magnetism and Magnetic Materials. 485, 140 – 144 (1995)

14. T.G.S.M. Rijks, R. Coheoorn, J. T. F. Daemen, and W. J. M. de jonge, J. Appl. Phys. 76, 1092 (1994)

15. L. H. Van Vlack, Elements of Materials Science and Engineering 6^{th}, Addison-Wesley Publishing Company (1989)

16. F. A. Cotton, G. Wilkinson, Advanced inorganic chemistry 5^{th}, Wiley-Interscience (1988)

17. O. Milton, The materials science of thin films, Boston Academic Press (1992)

18. T. Kodas, M. Hampden-Smith, The Chemistry of Metal CVD, VCH Publisher Inc, (1994)

19. G. McGuire, S. Rossnagel, and R. Bunshah, Handbook of Thin Film Deposition Processes and Technology, Second Edition, Noyes Publications (2002)

20. D. B. Rogers, R. D. Shannon, A. W. Sleight, and J. L. Gillson, Inorganic Chemistry. 8, 841 (1969)

21. W. Desisto, P. Broussard, T. Ambrose, B. Nadgorny, and M. Osofsky, Applied Physics Letters. 76, 3789 (2000)

22. K. Kamper, W. Schmitt, and G. Guntherodt, Phys. Rev. Lett. 24, 2788 (1987)

23. A. Gupta, X. W. Li, S. Guha, and G. Xiao, Applied Physics Letters. 75, 2996 (1999)

24. K. Suzuki, P.M. Tedrow, Physical Review B. 58, 597 (1998)

25. H. Y. Hwang, S. W. Cheong, Science. 278, 1607 (1997)

26. L. Ranno, A. Barry, and J. Coey, J. Appl. Phys. 81, 5774 (1997)

27. S. Ishibashi, T. Namikawa, Japan J. Appl. Phys. 17, 249 (1978)

28. X. Li, A. Gupta, and G. Xiao, Applied Physics Letters. 75, 713 (1999)

29. X. Li, A. Gupta, T. McGuire, P. Duncombe, and G. Xiao, J. Appl. Phys. 85, 5585 (1999)

30. M.J. Hampden-Smith, T.T. Kodas, and A. Ludviksson, in Chemistry of Advanced Materials: An Overview, L.V. Interrante and M.J. Hampden-Smith, Eds., Wiley-VCH (1998), p. 168

31. D. Barreca, C. Massignan, S. Daolio, M. Fabrizio, C. Piccirillo, L. Armelao, and E. Tondello, Chem. Mater. 13, 588 (2001)

32. K. Kuribayashi and R. Ueyama, Thin Solid Films 295, 16 (1997)

33. T. Maruyama and Y. Ikuta, J. Mater. Sci. 28, 5073 (1993)

34. Y. Ji, G.J. Strijkers, F.Y. Yang, C.L. Chien, J.M. Byers, A. Anguelouch, G. Xiao, and A. Gupta, Phys. Rev. Lett. 86, 5585 (2001)

35. K.J. Schwarz, J. Phys. F. *16*, L211 (1986)

36. Baibich, et al., Phys. Rev. Lett., 61, 2472 (1988)

37. K. Suzuki, P.M. Tedrow, Phys. Rev. B. 58, 11597 (1998)

38. L. Ranno, A. Barry, and J.M.D. Coey, J. Appl. Phys. 81, 5774 (1997)

39. B. D. Cullity, Elements of x-ray diffraction 2nd, Addison-Wesley (1978)

40. Hong-Qiang Li, "AFM Introduction", 1997
http://www.chembio.uoguelph.ca/educmat/chm729/afm/introdn.htm

41. S. Y. Lee, R.S. Feigelson, Journal of Crystal Growth. 186, 594 (1998)

42. J.M. Lee, H.C. Shin, C.S. Hwang, H. J. Kim, and C.G. Suk, J. Vac. Sci. Technol. A. 16, 2768 (1998)

43. W.C. Shin and S. G. Yoon, Journal of the Korean Ceramic Society. 34, 241 (1997)

44. T. Takagi, I. Oizuki, I. Kobayashi, and M. Okada, Japan. J. Appl. Phys. 34, 4104 (1995)

45. J. Si, S. J. Desu, J. Mater. Res. 8, 2644 (1993)

46. S. E. Park, H. M. Kim, K.M. Kim, and S. H. Min, Thin Solid Films. 341, 52 (1999)

47. J. Sanker, T. Sham, and R. Puddephatt, J. Mater. Chem. 9, 2439 (1999)

48. P. Hones, T. Gerfin, and M. Gratzel, Appl. Phys. Lett. 67, 3078 (1995)

49. P. C. Liao, S. Y. Mar, W. S. Ho, Y. S. Huang, and K. K. Tiong, Thin Solid Films. 287, 74 (1996)

50. T. Maruyama, Y. Ikuta, J. Mater. Sci. 28, 5073 (1993)

51. H. Zang, H. Chang, J. Guo, and T. J. Zhang, J. Mater. Res. 9, 2264 (1994)

52. D. P. Partlow, S. R. Gurkovich, K. C. Radford, and L. J. Denes, J. Appl. Phys. 70, 443 (1991)

53. M. Sambi, M. D. Negra, G. Granozzi, Z. S. Li, H. Jorgensen, and P. Moller, Applied Surface Science. 142, 146 (1999)

54. M. Sambi, M. D Negra, G. Granozzi, Physical Review B. 55, 7850 (1997)

55. H. L. M. Chang, H. You, J. Guo, and D. J. Lam, Applied Surface Science. 48/49, 12 (1991)

56. F. Guinneton, L. Sauques, J. C. Valmalette, F. Cros, and J. R. Gavarri, Journal of Physics and Chemistry of Solids. 62, 1229 (2001)

57. F. Beteille, R. Morineau, J. Livage, and M. Nagano, Materials Research Bulletin. 32, 1109 (1997)

BIOGRAPHY OF THE AUTHOR

Youngnam Cho was born in Kyungju, Korea on October 12, 1974. She graduated from Sungnam women's high school in 1993. She entered the Dongguk University and graduated in 1997 with a Bachelor's degree in Chemical Engineering. She worked for LG-EDS company for 2 years as a system engineer. She came to Maine in August 2000 to obtain a Master of Science degree in Chemical Engineering.

After receiving her degree, Youngnam will attend Purdue University for a Ph.D degree in Chemistry. Youngnam is a candidate for the Master of Science degree in Chemical Engineering from The University of Maine in August, 2002.